Results in Engineering 29 (2026) 108711

Contents lists available at ScienceDirect

Results in Engineering

journal homepage: www.sciencedirect.com/journal/results-in-engineering

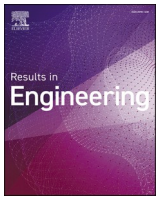

Research paper

Numerical evaluation of fibre anchor configurations in cfrp-strengthened concrete beams

Asal Pournaghshband [a,*], Mohammed A. Zaki [b]

[a] Centre for Engineering Research, School of Physics, Engineering and Computer Science, University of Hertfordshire, Hatfield, AL10 9AB, United Kingdom
[b] Department of Civil Engineering, American University in Dubai, Dubai, United Arab Emirates

ARTICLE INFO

Keywords:
Cfrp-strengthen beams
Finite element modelling
Anchor configurations
Beam geometry
Debonding failure

ABSTRACT

This study presents a detailed numerical investigation of beams strengthened with CFRP sheets and anchored using splay type fibre systems. Finite element models were developed in ABAQUS and validated against full scale tests with over 95 % accuracy in predicting ultimate load. The models reproduced the load–deflection behaviour and failure modes with high fidelity, supporting the parametric study. For T-section beams, the analysis examined embedment depth, anchor spacing, and end-anchor removal. For rectangular beams, it focused on embedment depth for two web sizes. In T beams, a 100 mm embedment depth prevented pull out and caused CFRP rupture, confirming full tensile mobilisation. An optimal 140 mm spacing maintained effective stress transfer, while wider spacing induced premature debonding. End anchors within 16 % of the shear span contributed negligibly, defining a non-effective anchorage zone. In rectangular beams, capacity plateaued with deeper embedment as early concrete crushing limited the mobilisation of the CFRP. Increasing the web depth from 305 mm to 350 mm produced only a minor capacity increase. These findings demonstrate that beam geometry strongly governs anchor performance and provide guidance for efficient CFRP strengthening design.

1. Introduction

To address the challenges of aging structures subjected to increased loads, environmental degradation, or physical damage, carbon fibre-reinforced polymer (CFRP) materials are commonly employed as a rehabilitation measure, applied to the tensile regions to enhance structural performance. Due to its lightweight, high strength, and corrosion resistance, CFRP is an exceptional reinforcement material, particularly well-suited for marine structures [1] and [2]. FRP materials are ideal for rapid rehabilitation and can be effectively bonded externally to concrete surfaces [3]. In addition to enhancing overall performance, CFRP can influence cracking behaviour and modify failure patterns in RC structures, resulting in improved structural performance and greater durability [4],[5], and [6]. Despite these enhancements, the overall effectiveness of CFRP is often constrained by common failure mechanisms. Failures typically occur due to the debonding of CFRP strips from the concrete substrate. Experimental evidence indicates that debonding typically initiates when the strip utilizes approximately 40 %−50 % of its tensile strength [7] and [8]. To fully harness the tensile strength of CFRP strips and mitigate premature debonding, CFRP fibre anchors are employed, typically with recommended embedment depths ranging from 130 to 150 mm [9]. Extensive research has underscored the critical role of FRP anchorage systems in preventing debonding and mitigating brittle failures in strengthened RC beams [10–16], and [17]. FRP debonding failure is brittle and occurs catastrophically at low structural deformations, presenting significant challenges for design. To mitigate this, guidelines like ACI 440.2R [18], TR55 [19], and CNR-DT200R1 [20] recommend incorporating anchorage systems to delay or prevent such failures. Building on these recommendations, many research projects have examined the use of U-wrap anchorage systems as an effective means to delay the premature debonding while simultaneously improving the flexural and shear capacity of reinforced concrete members [21–29], and [30]. In parallel, several studies have considered the use of fibre anchors, which have demonstrated significant enhancement in flexural and shear strength by controlling the premature bond failure.

Del Rey Castillo et al. developed a design methodology for FRP spike anchors in RC structures strengthened with CFRP [31]. Their study found that embedment depths between 17.5 mm and 100 mm effectively prevented concrete cone failure, with failures mainly attributed to dowel pullout and combined concrete-cone and bond failure modes.

* Corresponding author.
E-mail address: a.pournaghshband@herts.ac.uk (A. Pournaghshband).

https://doi.org/10.1016/j.rineng.2025.108711
Received 6 October 2025; Received in revised form 10 December 2025; Accepted 11 December 2025
Available online 12 December 2025

Similarly, Huang et al. studied RC beams strengthened with prestressed CFRP and H-type end anchors, focusing on ductility and impact resistance [32]. They determined that an embedment depth of six times the anchor diameter ensured effective load transfer. Consequently, failures were primarily flexural or caused by yielding of the screw rod in the anchorage system. The findings emphasize the importance of precise design and installation. In parallel, Assad et al. demonstrated that CFRP spike anchors effectively reduced debonding in CFRP laminates, improving load capacity and strain utilization [33]. They recommended embedment depths of six times the anchor diameter to prevent failure, which was otherwise primarily caused by anchor rupture or concrete cone failure. Likewise, Wang et al. experimentally evaluated RC frame joints strengthened with CFRP sheets using various anchorage methods [34]. Their tests showed that hybrid bolt-plate locking anchors were the most effective in reducing debonding and slip. The optimal embedment depth was determined to be six times the anchor diameter. Failures were observed as flexural failure in the beams and shear failure in the core region. Furthermore, Dong et al. conducted experimental and analytical studies on the bond behaviour between CFRP and concrete with FRP anchors [35]. They found that a 60 mm embedment depth significantly improved load transfer and reduced premature debonding. Failures were mainly caused by CFRP rupture and interface debonding. Additionally, Mhanna et al. conducted experimental tests on RC T-beams strengthened with CFRP U-wraps and spike anchors to enhance shear performance [36]. They found that a 75 mm embedment depth effectively prevented concrete-cone failure. Failures were mainly due to CFRP laminate debonding and partial anchor pullout. Anchored systems significantly improved shear capacity and strain utilization compared to unanchored configurations. Addressing detailed design considerations, Shekarchi et al. recommended detailed design guidelines for CFRP anchors [37]. They emphasized the importance of an anchor-to-strip material ratio (AMR) greater than 2.0 to achieve full material utilization. A chamfer radius of at least 1.4 times the anchor hole radius was also suggested to reduce stress concentrations and ensure effective performance.

Extending this line of research, Zaki et al., have extensively studied advancements in the performance of RC beams strengthened with CFRP. Their work highlights the effectiveness of various anchorage techniques in enhancing structural performance. Studies have demonstrated that optimized CFRP fibre anchors and splay anchor configurations significantly enhance flexural capacity and minimize debonding failures, with smaller anchors and closer spacing yielding better results [38],[39],. The use of innovative bidirectional U-wraps and fibre anchors has been proven to effectively increase strength and ductility, with efficient configurations minimizing material usage while achieving substantial performance improvements [40],[41], and [42].

Previous studies have demonstrated the benefit of CFRP anchors in enhancing the flexural performance of strengthened RC beams. However, the effect of beam section shape on anchor behaviour, CFRP mobilisation, and failure mode remains insufficiently explored. This gap extends to the influence of anchor embedment depth and layout on failure load and overall system performance. Differences in failure mechanisms between sections, particularly the limiting role of concrete crushing in deeper beams, are often overlooked. Moreover, anchors placed near beam ends may lie outside the active strain zone and contribute minimally, yet this non-effective region has not been clearly defined. Addressing these limitations through targeted evaluation is essential for developing efficient and reliable anchorage design strategies.

This study addresses these gaps using a validated FE modelling approach. Section 2 presents the development and calibration of the numerical model, which captures the nonlinear interaction between concrete, steel, CFRP sheets, and fibre anchors. Particular attention was given to modelling the bond interaction and failure mechanisms across multiple interfaces, which required high-fidelity input parameters for fracture energy, interfacial stress transfer, and material degradation. The validation process was extended to both T-section and rectangular-section beams to ensure broad applicability. Section 3 presents the results of a comprehensive parametric investigation. For T-section beams, the study evaluates the effects of anchor embedment depth, spacing, and end anchor removal on flexural performance. For rectangular beams, the analysis focuses on embedment depth for two section sizes to assess the role of beam geometry. The results define the embedment depth required to prevent pull-out failure, establish the spacing limit beyond which debonding governs, and identify the regions where anchor placement does not contribute to capacity. Section 4 summarises the key findings and provides guidance for the design of CFRP anchor systems. The outcomes support more efficient material use while ensuring reliable structural performance in CFRP-strengthened concrete beams.

2. Development of numerical modelling and validation

2.1. General

To assess the flexural behaviour of reinforced concrete beams strengthened with CFRP laminates and splay-type fibre anchors, advanced Finite Element (FE) modelling was carried out using ABAQUS 2023, version 2023 [43]. The modelling process commenced with a rigorous validation phase, in which the numerical model was benchmarked against established experimental and computational results. Specifically, reference was made to three full-scale T-beams, and three full-scale rectangular beams previously tested by Zaki et al. [38], which incorporated CFRP U-wraps anchored using fibre anchors systems. Following successful validation, the models were employed to perform extensive parametric analyses. The development and validation of the FE models are thoroughly addressed, ensuring their accuracy and reliability for conducting these advanced analyses in Section 2.

2.2. Test plan

The numerical models developed in this study were validated by comparing them with experimental results reported in the literature. The computational analysis, carried out by the same authors, applied an Excel-based program to evaluate each beam [38]. The experimental analysis used for this numerical validation focused on the flexural performance of both rectangular and T-section beams strengthened with CFRP sheets and anchored using fibre anchors. In all cases, beam geometries were precisely defined with a total length of 4.88 m A shear span of approximately 1.75 m was used for four-point bending tests to enable a comprehensive evaluation of flexural behaviour. For the rectangular beams, specimens were cast with a width of 152 mm and a depth of 305 mm, while the T-beams maintained the same web dimensions but included a flange width of 406 mm and a thickness of 102 mm, Fig. 1-(a-b).

The beams were cast using ready-mix concrete with a 28-day compressive strength of 38 MPa and a measured modulus of elasticity of 29.2 GPa. The steel reinforcement exhibited a yield strength of 488 MPa for the tension bars and 470 MPa for the compression bars, with corresponding modulus of elasticity of 211 GPa and 200 GPa.

To enhance the flexural capacity of the beams, CFRP sheets were externally bonded using a high-strength epoxy adhesive. Four CFRP sheets were installed on the tension side of the beam that consisted of three layers of unidirectional CFRP sheets (C100) and one layer of bidirectional CFRP sheet (C220B). The first two C100 layers were applied only to the bottom (tension) face of the beams, while the third C100 layer extended 51 mm up both sides from the soffit to improve anchorage. Subsequently, one layer of bidirectional CFRP (C220B) was applied over the previous layers and wrapped 89 mm up the sides, as illustrated in Fig. 1 (c-e). The unidirectional sheets had a tensile strength of 966 MPa, a tensile modulus of 66.19 GPa, and a thickness of 0.584 mm, while the bidirectional sheets had a tensile strength of 1068 MPa, a tensile modulus of 96.53 GPa, and a thickness of 0.51 mm. Fig. 1

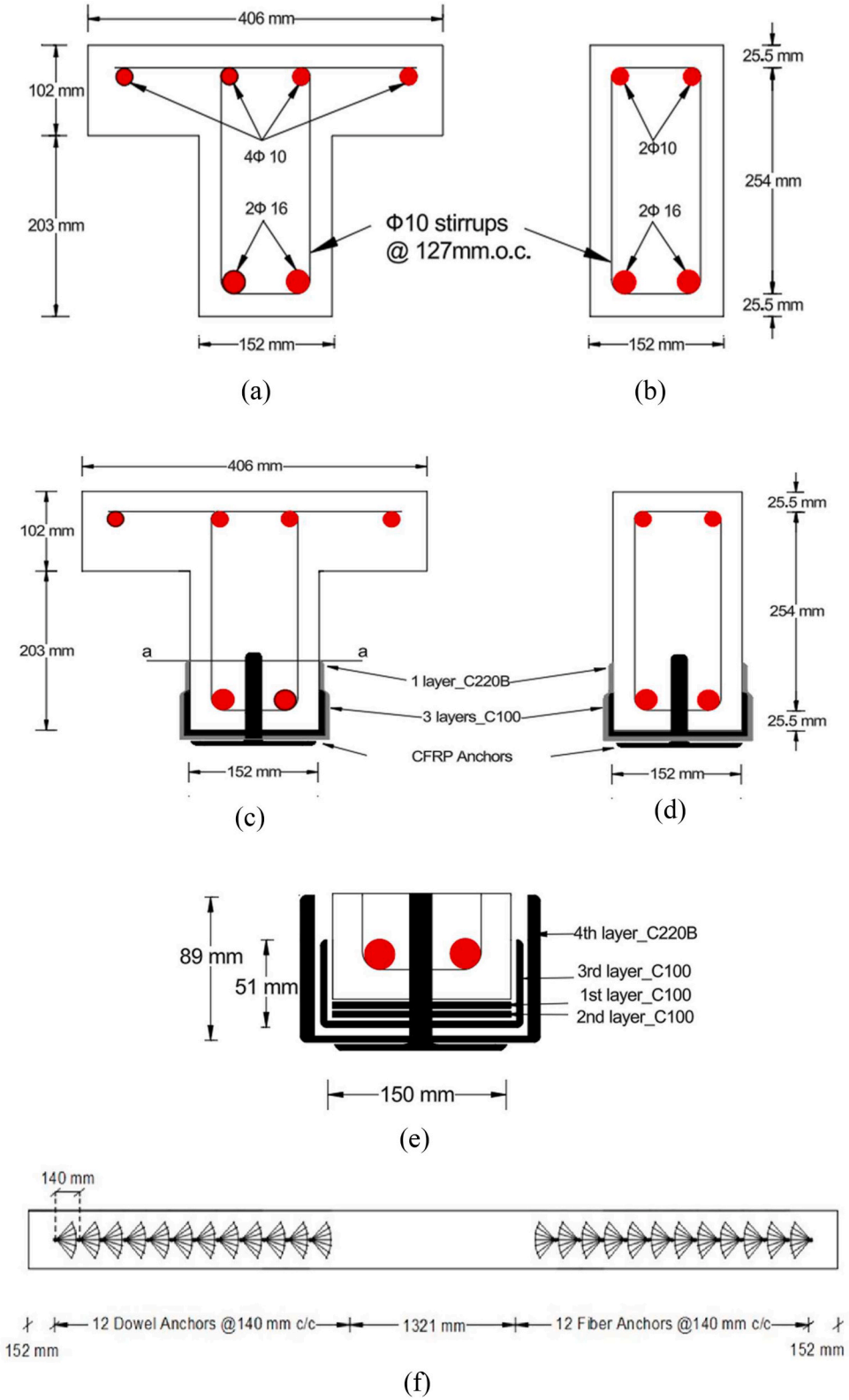

Fig. 1. Cross-sections and strengthening details of the tested beams: (a) T-beam cross-section with reinforcement; (b) Rectangular beam cross-section with reinforcement; (c) T-beam CFRP sheet configuration; (d) Rectangular beam CFRP sheet configuration; (e) Detailed CFRP sheet layout; and (f) Schematic layout of 16-mm-diameter CFRP anchors.

illustrates the internal reinforcement arrangement for both beam types along with the configuration of the CFRP sheets and fibre anchors. Two anchorage layouts were investigated: one using 19 mm diameter anchors spaced at 203 mm and another using 16 mm diameter anchors spaced at 140 mm, corresponding to nine and twelve anchors per shear span, respectively. The layout with 16 mm anchors is illustrated in Fig. 1 (e) to represent the anchorage configuration. Also, Table 1 provides the identification and layout of the tested specimens.

Table 1
Specimen identifiers and configurations.

Specimen ID	Description
CBT	Control beam with T-shaped cross-section, no strengthening.
SB16ST	T-beam, strengthened with CFRP sheets and 16 mm fibre anchors.
SB19ST	T-beam, strengthened with CFRP sheets and 19 mm fibre anchors.
CBR	Control beam with rectangular cross-section, no strengthening.
SB16SR	Rectangular beam, strengthened with CFRP sheets and 16 mm fibre anchors.
SB19SR	Rectangular beam, strengthened with CFRP sheets and 19 mm fibre anchors.

The tests were conducted under displacement-controlled four-point bending using a hydraulic actuator and steel loading frame, shown in Fig. 2. Load was applied symmetrically at a rate of 2.54 mm/min. Mid-span deflections were captured using LVDTs, and strain development was monitored through electrical resistance strain gauges installed at critical points. These included the top compression face, longitudinal reinforcement, CFRP sheets, and selected fibre anchors. Data collection focused on capturing both global flexural response and localised behaviours such as debonding, pull-out, and anchor shear.

2.3. Prior computational model

Building on the experimental tests described earlier, a computational analysis was performed using an Excel-based program developed at Kansas State University. This program was utilized to predict the load-deflection and load-strain behaviour of the tested beams, along with critical flexural parameters such as ultimate capacity, failure modes, and moment-curvature relationships. The analysis employed an incremental deformation technique, progressively increasing the extreme compression fibre strain from zero to 0.003. For each strain increment, iterative calculations determined the neutral axis depth under force equilibrium, enabling the computation of the corresponding moment-curvature points. Additionally, the load-deflection response was derived by numerically integrating the deflection expression across 50 segments of the shear span using the moment-curvature data. This computational analysis served as a vital tool for evaluating the experimental results.

2.4. Development of FE models

The numerical models for this study were developed using ABAQUS [43], incorporating a detailed representation of material behaviour, boundary conditions, and interaction properties to simulate the structural response under applied loading. The analyses focused on capturing the interaction between concrete, CFRP laminates, and steel reinforcements, alongside the behaviour of anchors securing the CFRP.

2.5. Mesh configuration

A mesh sensitivity analysis was conducted to balance accuracy and computational efficiency. The same mesh strategy was used for both the rectangular and T-section beams. Concrete and CFRP were meshed with C3D6 tetrahedral elements. Steel reinforcement used T3D2 truss elements, and CFRP laminates were modelled with S4R shell elements. Mesh sizes of 40 mm, 35 mm, 30 mm, and 25 mm were assessed. The 40 mm mesh underestimated load capacity and stiffness, while 35 mm improved accuracy. A 30 mm mesh offered stable results with minimal gains beyond this size. To demonstrate this, Fig. 3. presents the comparative load-displacement and load-strain responses for specimen SB16ST. The results show that further refinement below 30 mm produced negligible differences in stiffness and ultimate capacity, confirming mesh convergence. The selected mesh therefore ensured reliable prediction of global and local responses while maintaining computational efficiency.

Thus, 30 mm was selected for the concrete and CFRP domains. A finer 10 mm mesh was applied around anchors and drilled holes to capture local cracking and interface behaviour, ensuring accurate simulation of stress concentrations and local failure. The selected mesh configuration produced approximately 12 to 13 elements across the beam width of 402 mm, corresponding to 22 integration points. Along the height of 305 mm, the mesh yielded approximately 13 to 14 elements, corresponding to 14 integration points. In critical regions near anchors and openings, the mesh was refined to 10 mm, increasing the element density accordingly. These values are consistent with established practice. For reference, eight elements across a 150 mm width were used by [44], equivalent to a 19 mm mesh, and [45] applied seven elements across a 170 mm depth, corresponding to a 24 mm mesh. The present element density is therefore comparable to or finer than those reported in previous studies.

2.6. Boundary conditions and loading

The supports and load application points in the numerical model were linked to designated reference points using *KINEMATIC coupling to replicate the experimental setup with high accuracy. At the left support (RP-2), all translational degrees of freedom (U_x, U_y, U_z) and rotational degrees of freedom, except rotation about the X-axis (R_x), were constrained. The right support (RP-1) was constrained in translational directions U_x and U_y, allowing free translation along the Z-axis and rotation about the X-axis to replicate the experimental boundary conditions accurately.

The analysis was displacement-controlled, matching the experimental setup and enabling accurate simulation of post-peak behaviour. The simulation was terminated once complete load drop occurred and full debonding or crushing was reached, indicating global failure of the beam. To simulate the loading condition, displacement was applied at

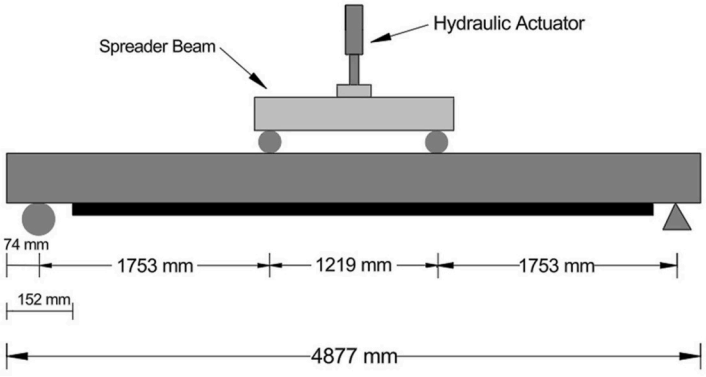

Fig. 2. Specifications of the beam and experimental test configuration.

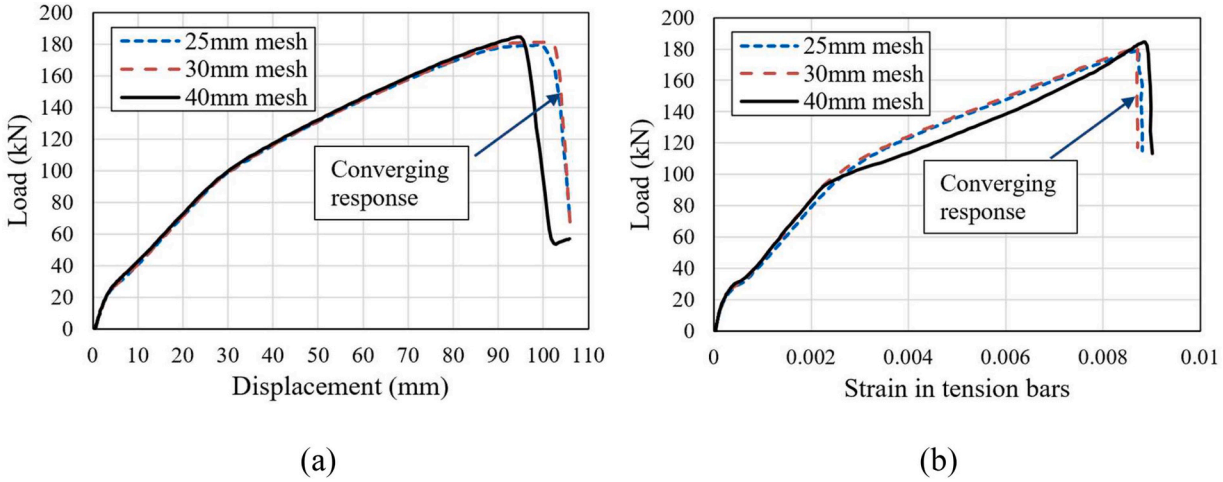

Fig. 3. Comparison of load–displacement and load–strain responses from the mesh sensitivity analysis for specimen SB16ST: (a) load–displacement response; and (b) load–strain response in tension bars.

the top reference points (RP-3 and RP-4). The reaction forces at these nodes and the vertical displacements at mid-span were recorded to generate force-displacement curves. To avoid stress concentration at the supports and load points, node coupling was extended to three rows around each reference point. This approach replicated the behaviour of a rigid loading plate. The contact area spanned 60 mm, equal to twice the adopted 30 mm mesh size. This treatment helped spread the load uniformly and improved solution stability. The configuration of supports, loading points, and mesh layout is shown in Fig. 4 for both the T-section and rectangular beams.

2.7. *Material properties*

The stress-strain relationship for steel was modelled following Yun

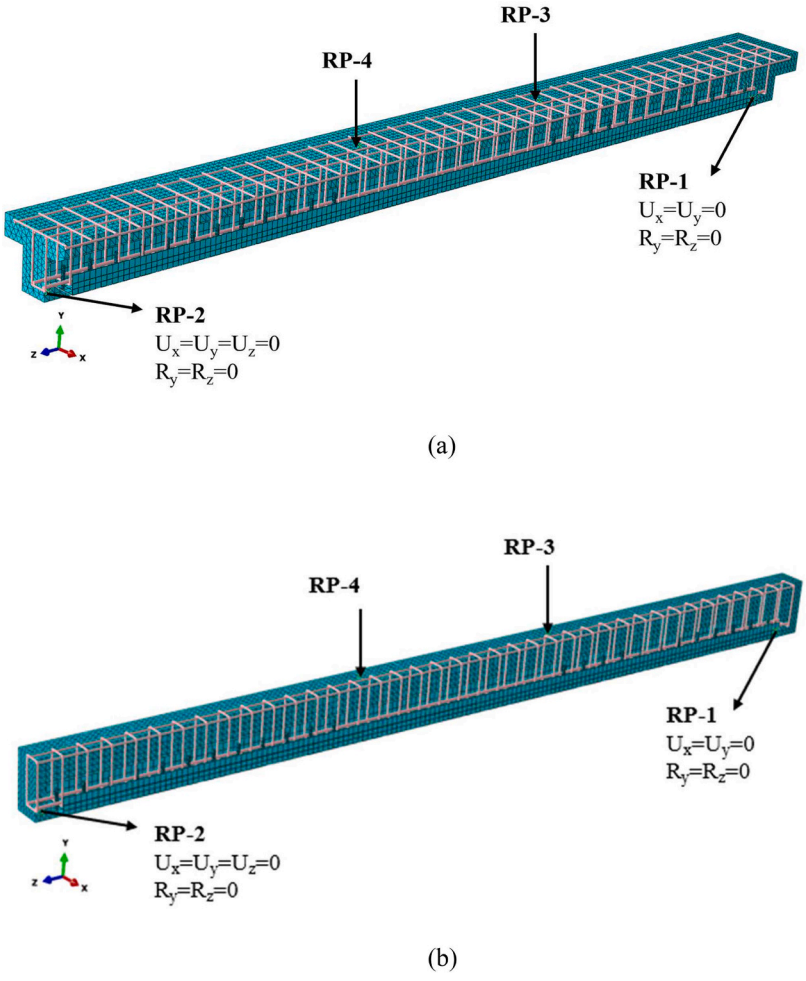

Fig. 4. Configuration of boundary conditions and mesh in the numerical model for (a) T-section beam; and (b) rectangular-section beam.

and Gardner [46], incorporating experimentally measured material properties. The model captures the elastic region, yield plateau, and strain hardening. The onset of strain hardening occurs at strain ε_{sh}, which is predicted using an empirical equation dependent on the yield-to-ultimate stress ratio (f_y/f_u), ensuring material-grade-specific accuracy. Plastic behaviour was defined using a bilinear plus nonlinear hardening model, which accounts for progressive stiffness reduction beyond yielding [18]. Fig. 5 presents the proposed stress-strain model used in this study, comparing the experimental stress-strain curve with the bilinear plus nonlinear hardening model by [46]. The proposed model, calibrated against experimental data, accurately captures elastic behaviour, yielding, and strain hardening. Its nonlinear hardening formulation improves predictive accuracy, making it suitable for advanced simulations [47].

The elastic modulus (E), yield strength (f_y), and ultimate strength (f_u) were determined from experimental data as 211 GPa, 488 MPa, and 755 MPa for the flexural steel, respectively, and 200 GPa, 470 MPa, and 735 MPa for the top steel bars. To accurately represent the nonlinear material behaviour, the true stress (σ_{true}) and logarithmic plastic strain $\left(\varepsilon_{\ln}^{pl}\right)$ were incorporated into the numerical model. These parameters were derived from the engineering stress (σ_{nom}) and strain (ε_{nom}) using the following equations:

$$\sigma_{true} = \sigma_{nom}(1+\varepsilon_{nom}) \tag{1}$$

$$\varepsilon_{\ln}^{pl} = \ln(1+\varepsilon_{nom}) - \frac{\sigma_{true}}{E} \tag{2}$$

Steel reinforcement was embedded into the concrete domain using the *EMBEDDED ELEMENT* constraint available in ABAQUS, ensuring full displacement compatibility between the host and embedded regions.

The concrete material model used a plasticity-based continuum damage approach to simulate uniaxial compressive and tensile behaviour. The damaged plasticity framework defined the material response, with the stress-strain curve showing linear elasticity under uniaxial tension up to the failure stress, as outlined in the ABAQUS user guide [43]. Beyond the failure point, stress induced micro-crack formation in the concrete matrix, representing progressive damage. Concrete properties were modelled using the*CONCRETE DAMAGED PLASTICITY (CDP) model in ABAQUS. This model captures stiffness reduction under tensile cracking and compressive crushing. An average compressive strength of 38 MPa and a Young's modulus of 29.2 GPa were defined based on experimental data. A Poisson's ratio of 0.2 was assumed, following ACI guidelines [18]. CDP plastic parameters were set according to the recommendations by [47]. A dilation angle of 35° and an eccentricity of 0.1 were adopted. The ratio of the second stress invariant on the tensile to compressive meridian was set to 1.16. The biaxial-to-uniaxial compressive strength ratio was taken as 2/3. Compressive stress-strain behaviour was defined using established relationships by [48]. The equation captures both the ascending and descending branches of the stress-strain curve. It accounts for compressive strength, peak strain, and an empirical material factor, ensuring broad applicability. For tension, the stress-strain behaviour was modelled using a serpentine curve similar to that used in compression, as suggested by [49]. Tensile behaviour was defined by tensile strength, peak strain, and a material-specific factor. The model captures the effects of cracking, bond slip, and reinforcement interaction, providing an accurate representation of reinforced concrete in tension. The stress–strain relationships used in the Abaqus simulations are shown in Fig. 6. The compressive strain range extended up to 0.20 and the tensile strain up to 0.002, consistent with the input data applied in the numerical modelling. However, for clarity of presentation, the compressive curve in Fig. 6(a) is truncated at 0.01 to better illustrate the pre-peak and early post-peak response; beyond this range, the curve continues smoothly with a gradual stress decay.

The material properties of the cured CFRP laminate sheets (C220B and C100) were obtained from manufacturer data. The elastic modulus (E) is 96,527 MPa for C220B and 66,190 MPa for C100. Their ultimate strengths (f_u) are 1068 MPa and 966 MPa, respectively. Poisson's ratio (ν) was determined using the rule of mixtures, with values of $\nu = 0.3$ for the epoxy resin and $\nu = 0.28$ for the laminate. The elastic properties were assumed isotropic due to the dominant tensile loading. Fracture behaviour was modelled using the Hashin damage criterion, incorporating longitudinal tensile strength and fracture energy (G_f). The Hashin failure model was used to describe damage initiation in the CFRP laminates. It evaluates fibre tension, fibre compression, matrix tension, and matrix compression separately using stress-based criteria. Failure occurs when the stress state in any mode exceeds its limit. After damage initiation, stiffness and strength degrade progressively according to a linear damage evolution law. This evolution is defined by the fracture energy required to reach complete failure. This approach captures the anisotropic and mode-dependent failure behaviour of CFRP with high accuracy. The fracture energy (G_f) was computed based on the values provided in Table 9 of [50]. G_f was determined by integrating the area under the stress-strain curve shown in Fig. 7 up to the point of ultimate tensile strength of each laminate. In Fig. 7, the initial (pre-damage) linear segment of the traction–separation law is defined by three stiffness parameters of K_{nn} in the normal direction, and K_{ss}, K_{tt} in the two orthogonal tangential directions. Since the epoxy adhesive is isotropic, the tangential stiffnesses are equal. These values determine the slope of the elastic response before damage initiates in tension (Mode I) and shear (Modes II and III). The integration assumed constant failure strain across laminates to ensure a consistent measure of fracture energy. Fig. 7 illustrates the bilinear traction-separation model from [50] capturing interfacial stiffness degradation from elastic response to damage

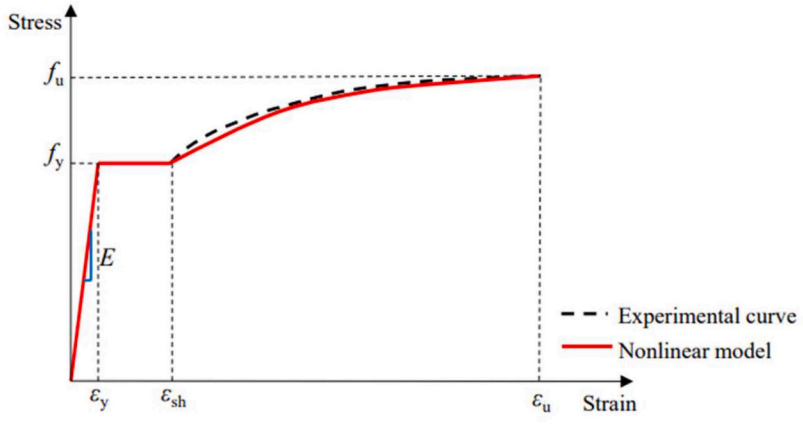

Fig. 5. Proposed bilinear plus nonlinear hardening model together with typical experimental stress-strain curve from [46].

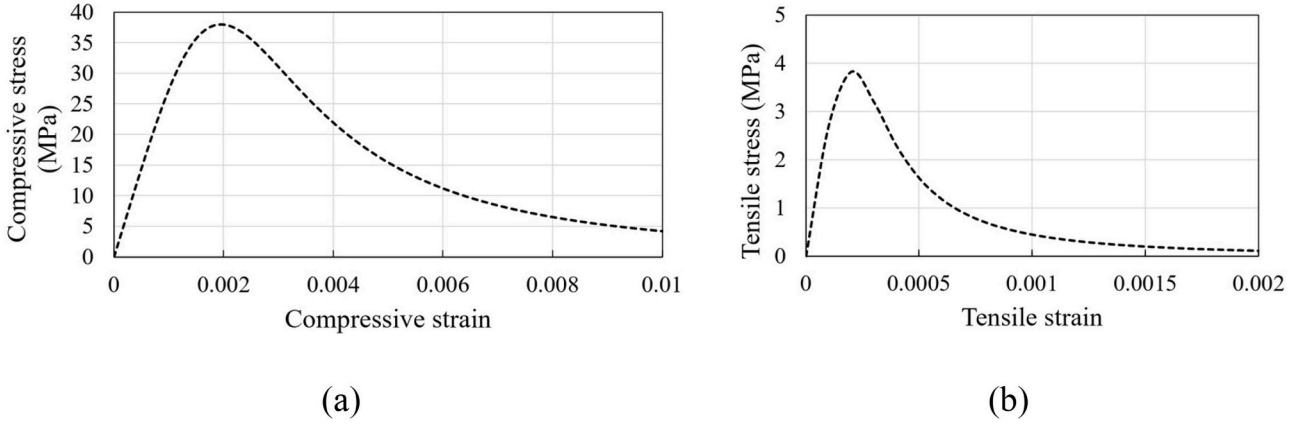

Fig. 6. Stress-strain behaviour of concrete (a) in compression; (b) in tension.

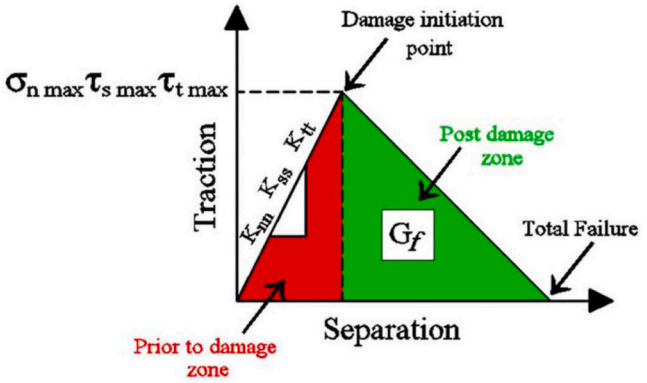

Fig. 7. Bilinear traction-separation model used to define the interfacial surface from [50].

initiation and eventual debonding.

The anchor was modelled as an orthotropic elastic composite to capture directional stiffness and failure. Damage was defined using the Hill yield criterion, with longitudinal and transverse strengths of 834 MPa and 60.7 MPa, respectively, based on manufacturer data. Transverse shear strength was taken as 6 % of the dry fibre tensile capacity, giving 79.3 MPa, based on [51]. Elastic properties, including longitudinal, transverse, and shear moduli, were calculated using the rule of mixtures. The fibre volume fraction was estimated based on manufacturer-provided dry and cured laminate data. Shear damage was modelled using parameters extracted from manufacturer data, with a fracture strain of 1.7 % and fracture energy of 21.83 Nmm/mm^2. Unlike the CFRP sheets, which were assumed isotropic, an orthotropic formulation was required for the anchors. FE analysis showed that transverse and shear stiffness significantly affected anchorage efficiency and delamination resistance. Fibre–matrix interaction in smaller anchors also influenced load transfer, requiring refined modelling for consistency with experimental results.

2.8. Interaction modelling

Steel and concrete interaction was modelled using *EMBEDDING constraints to ensure proper force transfer. This approach ensured full bond and strain compatibility between the reinforcement and surrounding concrete. Slip was not considered, which is consistent with standard modelling practice for internally cast reinforcement. *TIE constraints defined the contact between CFRP and anchors. A cohesive-zone model using *COHESIVE CONTACT was applied at the interfaces between CFRP and concrete and between anchors and CFRP. This approach simulated bond–slip behaviour under load. It also captured progressive debonding and eventual pull-out failure. Cohesive contact parameters, including initial stiffness, fracture energy, and local shear strength, were calculated using established models by [52]. The adhesive layer was assigned a thickness of 1.0 mm. The cohesive contact properties between CFRP sheets and the beam were defined based on stiffness parameters in the normal and tangential directions. The normal stiffness (K_{nn}) was set to 2760 N/mm, equivalent to the elastic modulus of the epoxy adhesive, while the tangential stiffness (K_{tt}) was taken as 1794 N/mm. The initial stiffness of the adhesive interface was calculated from the elastic modulus and thickness of the adhesive layer using a linear elastic equation provided by [50]. This defined the slope of the traction–separation law prior to damage initiation. For the adhesive and anchor interfaces, damage was modelled using cohesive zone laws. Once stresses exceeded the defined traction–separation limits, progressive stiffness degradation occurred, resulting in debonding or anchor pull-out. The strength in the normal direction was assigned as 3.8 MPa, corresponding to the tensile strength of concrete, ensuring consistency in modelling adhesive-concrete interaction. The shear strength (τ_{max}) was established as 1.1 MPa, while the fracture energy (G_f) was set to 0.45 Nmm/mm^2. These values were calibrated through multiple FE simulations to replicate experimentally observed failure mechanisms and force-strain behaviour. The selected shear strength and fracture energy align well with previous literature, including studies by [44], [45], and [50], which report shear strengths varying between 0.7 MPa and 3.0 MPa and fracture energy values ranging from 0.3 N.mm/mm^2 to 1.5 N.mm/mm^2. The anchor–beam interface showed stronger interlocking than the CFRP–beam interface. Based on [53], both shear and normal strengths were set to 5.8 MPa, with a fracture energy of 1.5 N.mm/mm^2. These parameters ensured accurate modelling of interaction and failure in CFRP-strengthened beams [54].

2.9. Validation of FE models

Comprehensive comparisons between experimental results, previous computational studies, and the FE simulations developed in this study are presented in Figs. 8–14 for the control T-beam (CBT) and the strengthened configurations SB16ST and SB19ST. Figs. 15–19 present corresponding results for the control rectangular beam (CBR) and the two strengthened configurations SB16SR and SB19SR. These figures depict the comparative load-deflection and load-strain responses at critical locations, including the top concrete surface, main reinforcing bars, and CFRP sheets. Additionally, failure modes observed in the experiments are compared with those predicted by the FE models for T-section beams, providing insight into the structural behaviour of CFRP-strengthened beams with fibre anchorages.

The results illustrate the ability of the developed FE models to

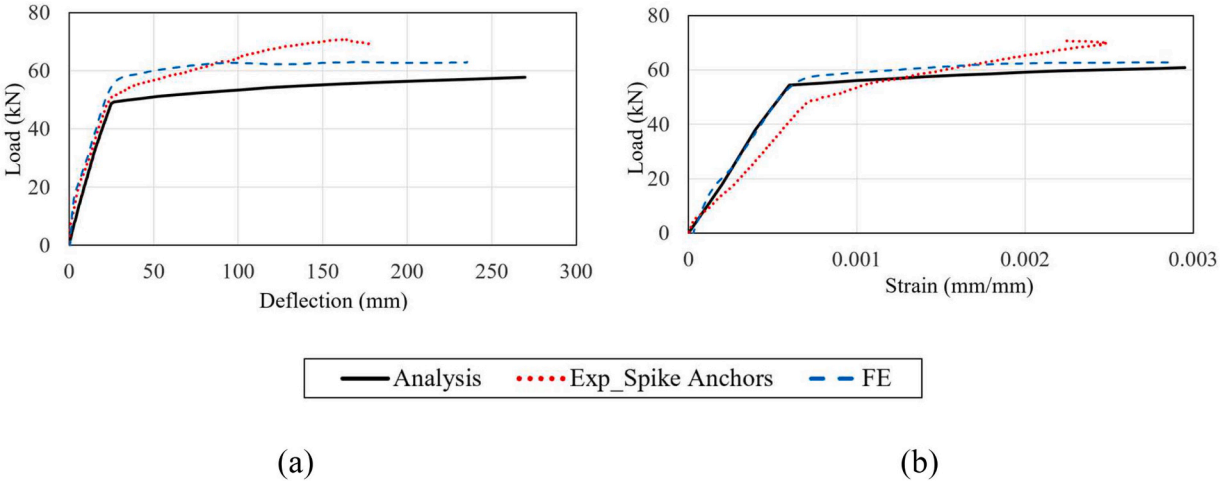

Fig. 8. Comparison between FE and literature [38] for (a) load-deflection of control beam CBT; and (b) load-strain at the top concrete surface of CBT.

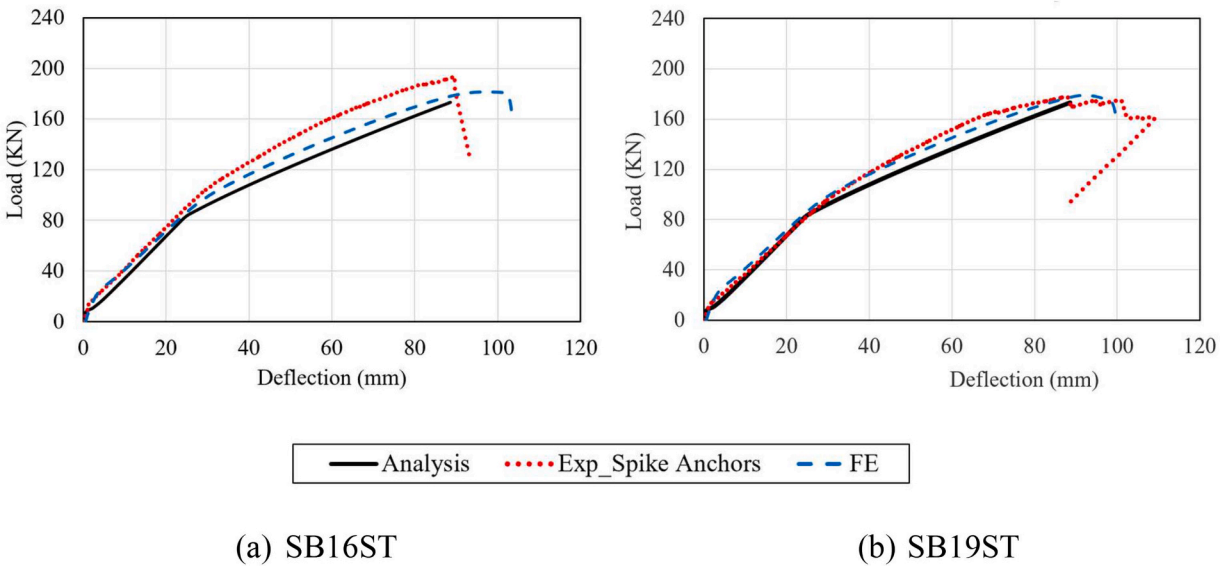

Fig. 9. Comparison between FE and literature [38] of load-deflection for (a) SB16ST beam; and (b) SB19ST.

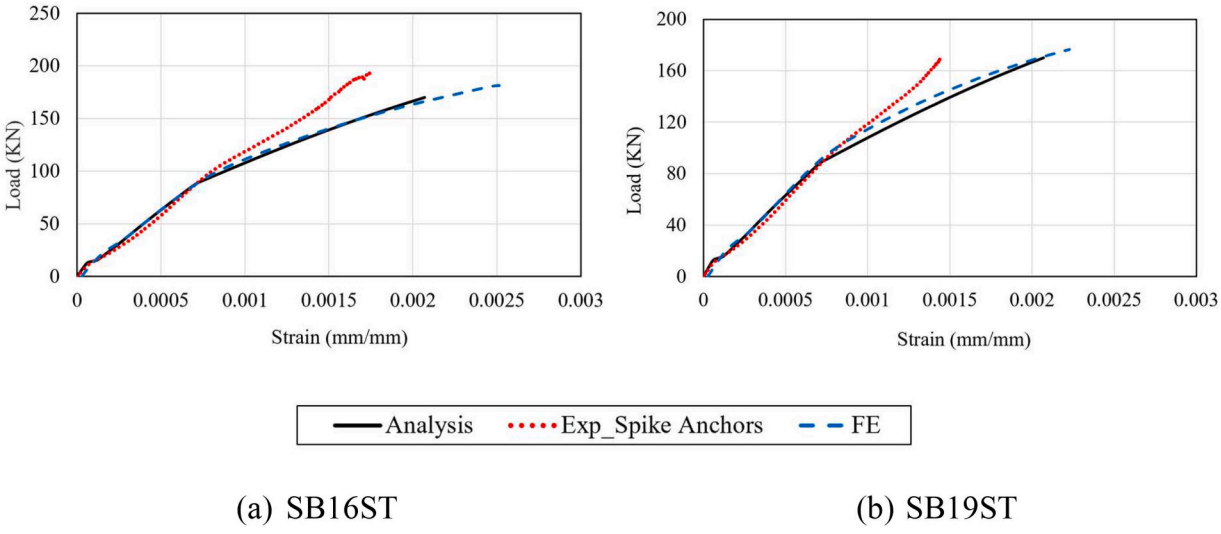

Fig. 10. Comparison between FE and literature [38] of the load-strain in the top concrete surface for (a) SB16ST beam; and (b) SB19ST.

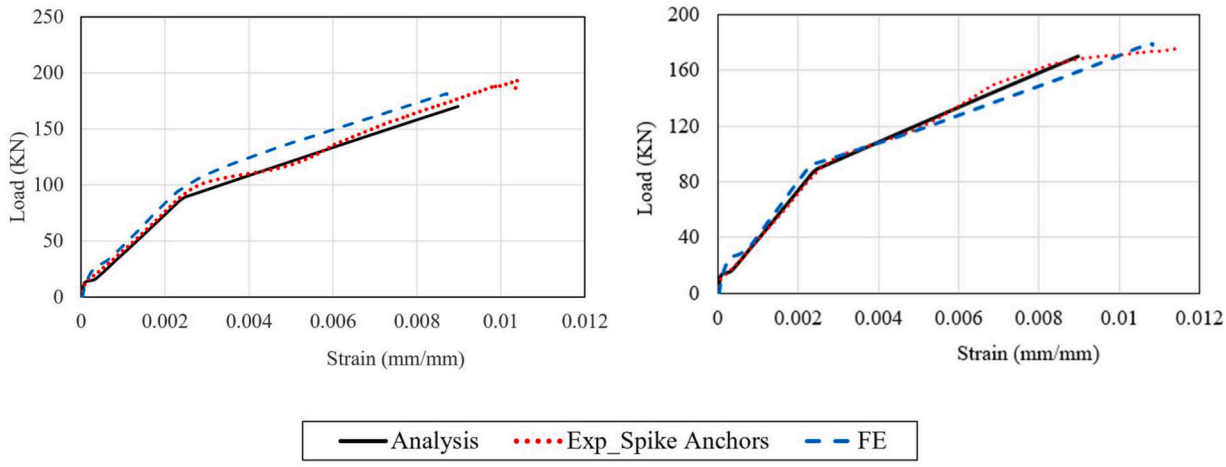

Fig. 11. Comparison between FE and literature [38] of the load-strain in the main rebars for (a) SB16ST beam; and (b) SB19ST.

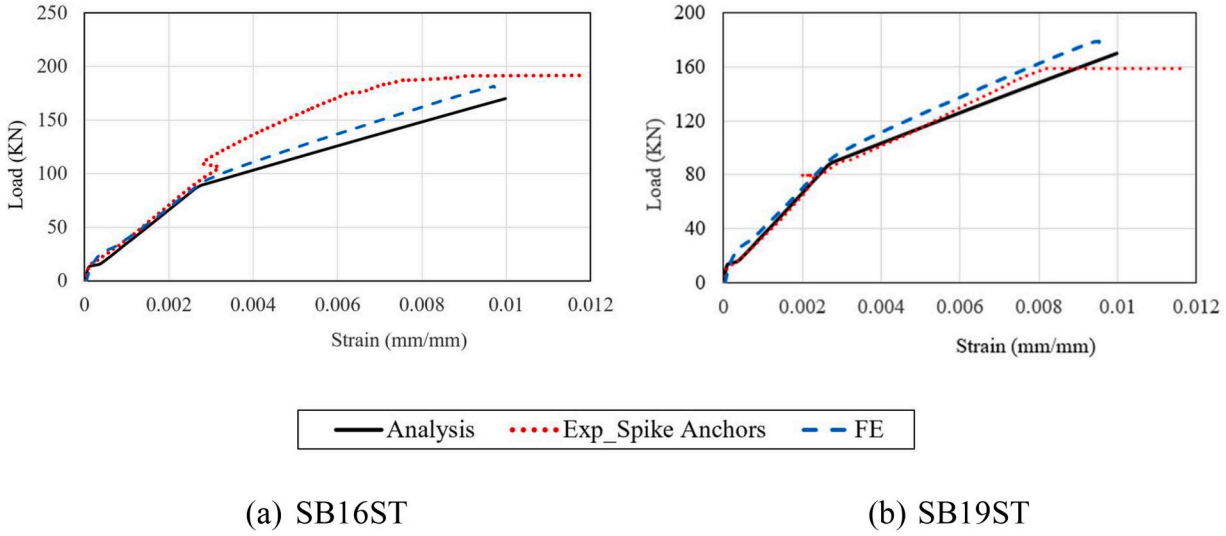

Fig. 12. Comparison between FE and literature [38] of the load-strain in the CFRP sheets for (a) SB16ST beam; and (b) SB19ST.

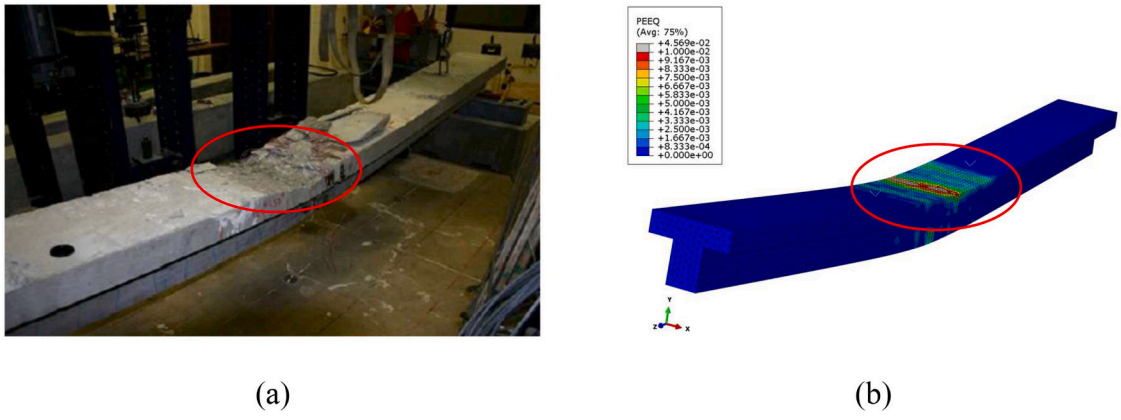

Fig. 13. Comparison of control beam CBT failure for (a) test; and (b) FE.

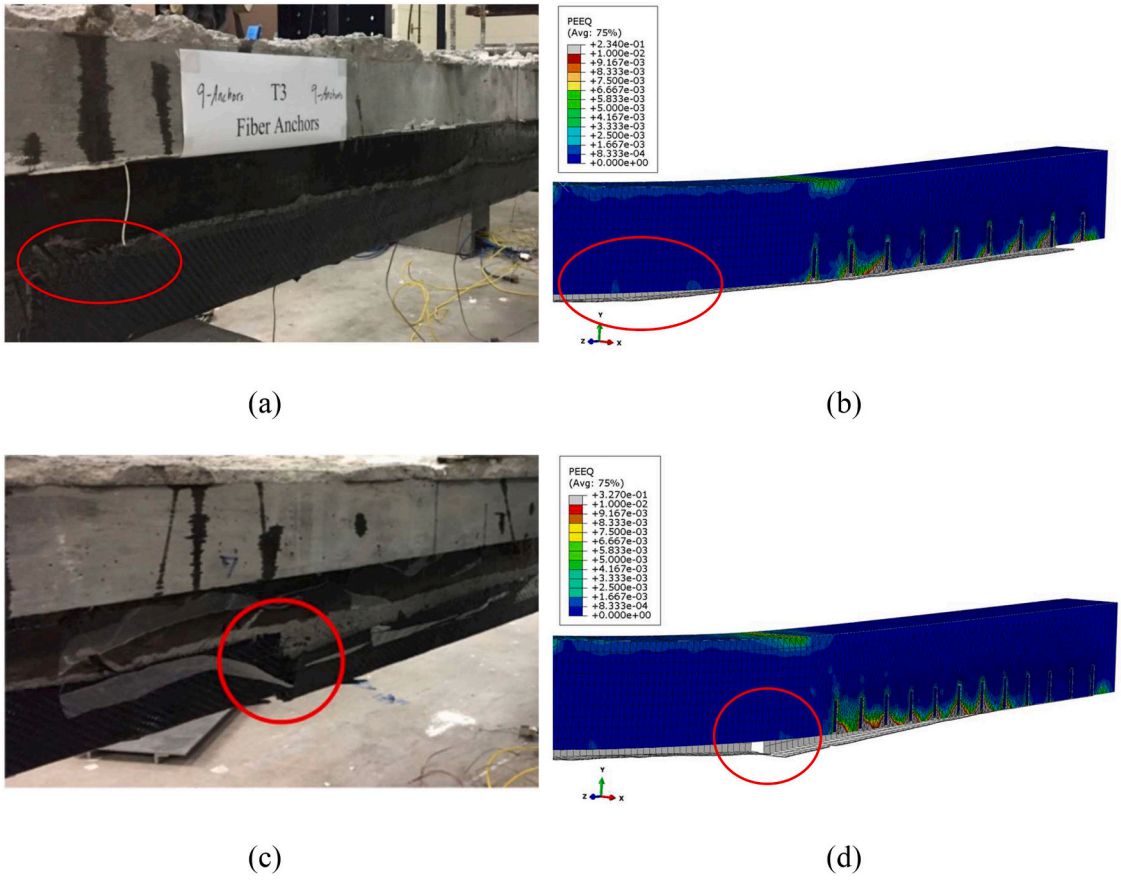

Fig. 14. Comparison of SB19ST beam after side CFRP debonding failure between (a) test; (b) FE; and SB16ST beam after rupture failure between (c) test and (d) FE.

replicate the force-displacement response with high fidelity. The numerical predictions closely follow the experimentally observed trends in stiffness, ultimate load capacity, and failure mechanisms, confirming the robustness of the numerical modelling approach. The model effectively captures the primary failure modes, with SB16ST exhibiting rupture-dominated failure, while SB19ST predominantly failed due to CFRP debonding. These failure characteristics are accurately reflected in the numerical results, as shown in Fig. 14.

To ensure accuracy, the developed numerical models were rigorously validated against experimental force-displacement data. The simulated results demonstrated a strong correlation with the experimental findings, reaffirming the reliability of the numerical framework. The ultimate load capacity predicted by the FE model for the T-section beam was 182.74 kN, which agrees with the experimental result of 193.4 kN reported in the earlier study [38] with an accuracy of approximately 95 %. Also, the predicted ultimate load capacity for the rectangular beam was 121.12 kN, which is within 97 % of the experimental value for the corresponding beam. This further confirms the validity of the numerical model. The consistency between numerical and test data supports the validity of the FE approach in predicting the structural behaviour of CFRP-strengthened beams. Despite the high degree of accuracy achieved, some unavoidable discrepancies between the numerical and experimental results are observed. These discrepancies stem from several factors, including the limited availability of material properties in the literature, reliance on derived data for input parameters, and inherent variability in experimental testing. Additionally, simplifications in the numerical representation of bond behaviour and material heterogeneity may contribute to slight deviations in the predicted response. Validation was based on a single experimental campaign to ensure consistency and control. All specimens shared identical materials, supports, and loading, removing external variability. The program included different beam sections, anchorage layouts, and failure mechanisms, allowing comprehensive verification within one framework. Model parameters such as fracture energy, bond strength, and interface properties were taken from experiments, standards, and validated literature. The model reproduced load–deflection behaviour, strain response, and failure modes across all cases without tuning. This approach aligns with established numerical practice and forms a robust basis for the parametric study in Section 3.

3. Parametric study and discussions

Following FE model validation, a focused parametric study was conducted to assess the effect of key anchorage parameters on the performance of both T-beams and rectangular beams.

3.1. *T-section beam parametric analysis*

The detailed study focused on the configuration with twelve anchors per shear span using 16 mm diameter anchors, as this arrangement demonstrated the highest performance and governed the local debonding behaviour between anchors [38]. The investigation examined the roles of embedment depth, anchor spacing, and end anchor removal. All models maintained the same geometry, materials, boundary conditions, and loading protocol as used in the validation phase. Material properties and interface definitions were calibrated to reflect observed behaviour. The study aimed to isolate each parameter and quantify its impact on load capacity and failure mode. Particular attention was given to debonding, pull-out, and rupture mechanisms. This approach allowed clear interpretation of results and identification of efficient anchorage configurations. The outcomes provide a foundation for improving the design of CFRP-strengthened concrete beams.

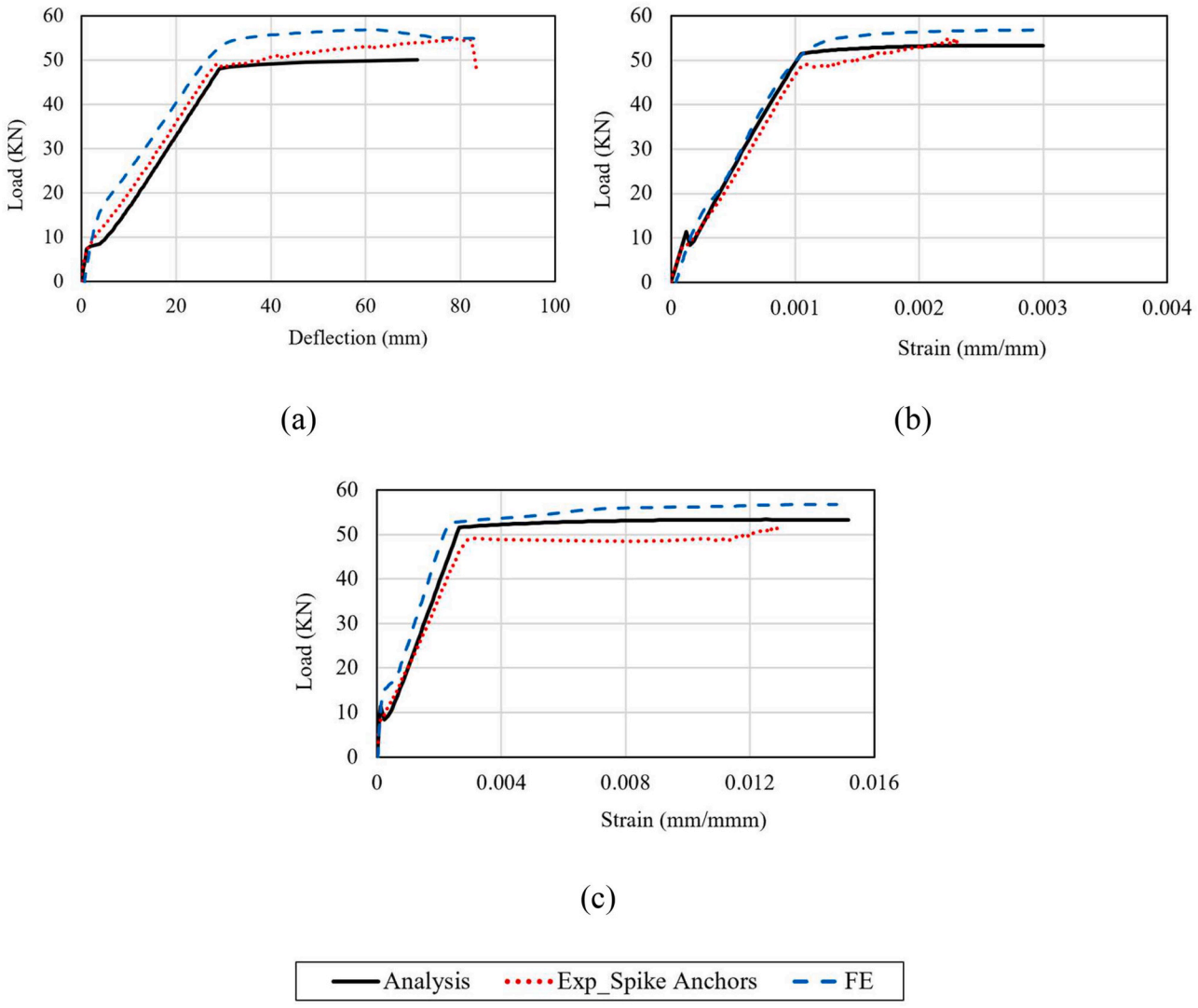

Fig. 15. Comparison of experimental, analytical, and FE results for the CBR: (a) load-deflection response; (b) strain at top concrete surface; (c) strain in main steel reinforcement.

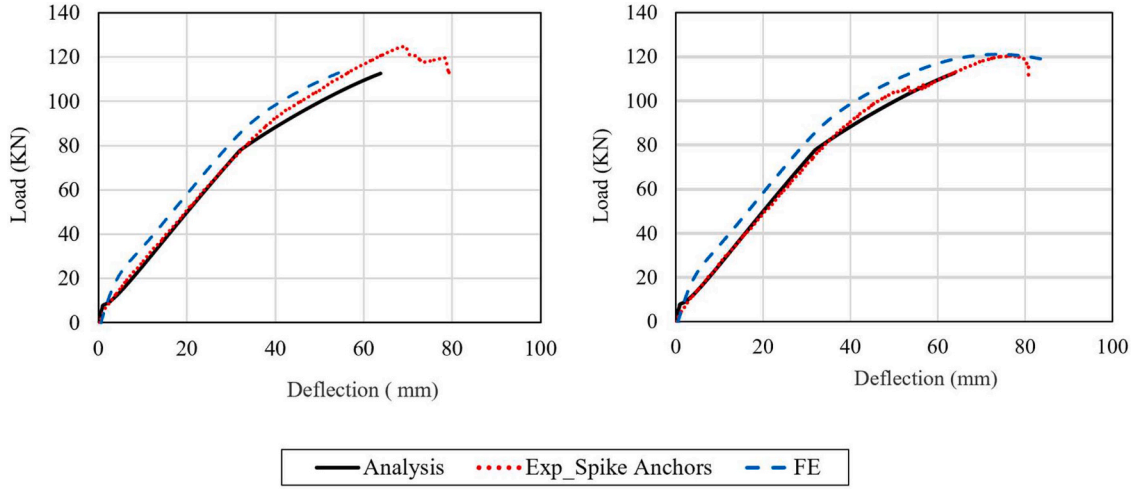

Fig. 16. Comparison between FE and literature [38] of load-deflection for (a) SB16SR beam; and (b) SB19SR.

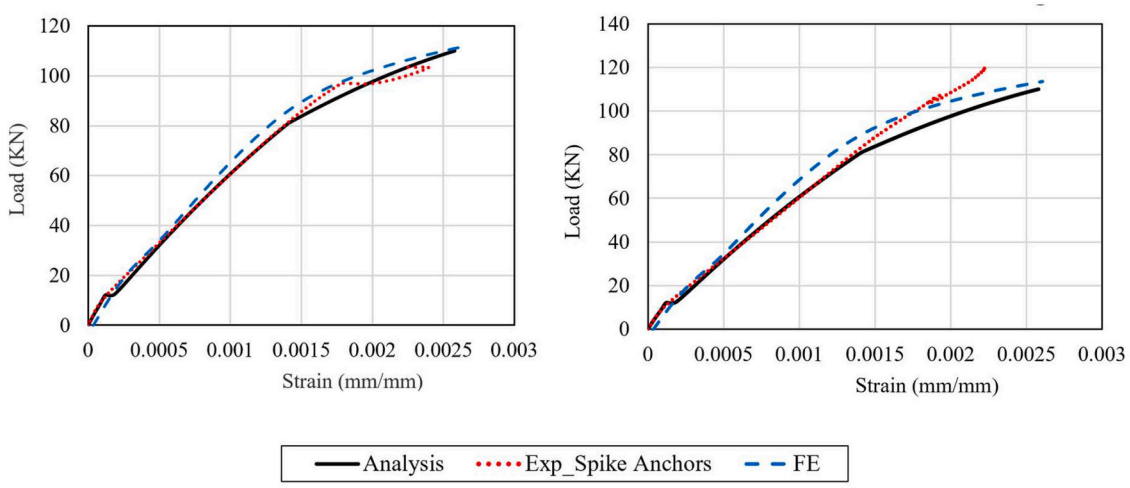

Fig. 17. Comparison between FE and literature [38] of the load-strain in the top concrete surface for (a) SB16SR beam; and (b) SB19SR.

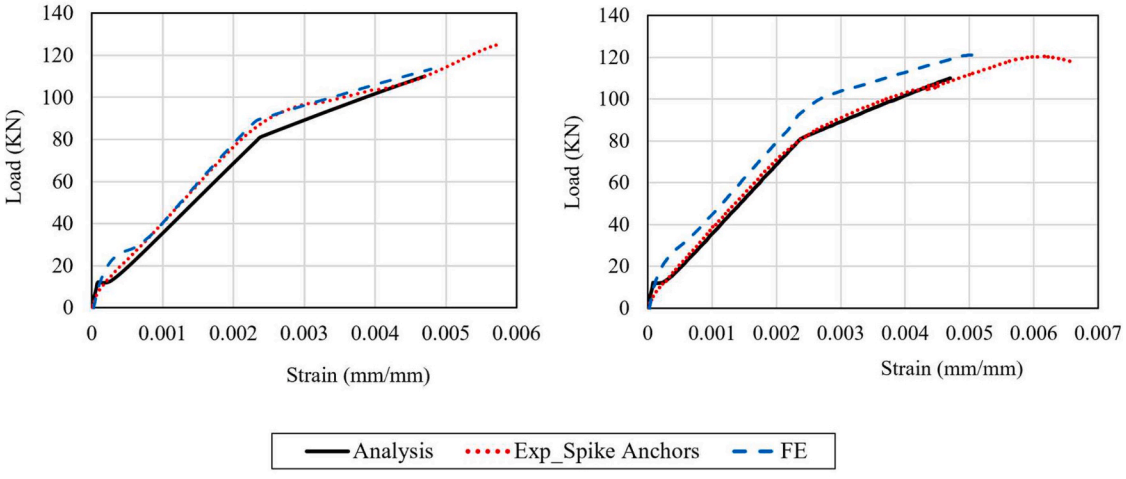

Fig. 18. Comparison between FE and literature [38] of the load-strain in the main rebars for (a) SB16SR beam; and (b) SB19SR.

3.1.1. Effect of embedment depth on performance

The embedment depth of CFRP fibre anchors plays a critical role in controlling load transfer and failure mechanisms. In this study, six different depths were examined: 30 mm, 40 mm, 60 mm, 80 mm, 90 mm, and 100 mm. Each depth was modelled in the validated FE framework to evaluate its influence on the beam's flexural response. The CFRP-strengthened T-beams were subjected to displacement-controlled four-point bending. The same anchorage layout, anchor diameter, and material properties were used in all cases to isolate the effect of embedment depth. For each model, the peak load and associated failure modes in both the CFRP sheet and the fibre anchors were recorded. The numerical analysis captured debonding, pull-out, and shear failures, depending on the depth used. Results are summarised in Table 2 and illustrated in Fig. 20. These findings provide a comparative understanding of how increasing embedment depth affects anchorage performance and overall beam strength.

To support the numerical findings presented in Table 2, Fig. 21 provides representative failure-mode visualisations for the SB16ST beam at embedment depths of 80 mm and 100 mm. These images illustrate the transition from CFRP sheet debonding at 80 mm to full CFRP rupture with at embedment depth of 100 mm, offering clear visual confirmation of the mechanisms predicted by the FE analysis.

The numerical results show a progressive increase in load capacity with increasing embedment depth, ranging from 30 mm to 100 mm. Depths of 30 mm, 40 mm, and 60 mm led to pull-out failures, indicating insufficient development length and ineffective stress transfer. The use of a shorter anchorage length reduces the bonded area between the CFRP sheet and the concrete, thereby limiting the transfer of tensile forces along the interface. As the anchorage length decreases, the load-carrying capacity of the beam correspondingly diminishes, approaching the debonding load observed in beams without anchors. This reduction in bonded length concentrates interfacial stresses over a smaller region, which may result in premature debonding, anchor pull-out, or an overall reduction in structural capacity. Insufficient anchorage length can therefore compromise the effectiveness of CFRP strengthening.

At 80 mm, failure involved both pull-out and shear, marking a transitional stage with partial anchorage engagement. At 90 mm, pull-out was eliminated and anchors failed in shear, reflecting improved

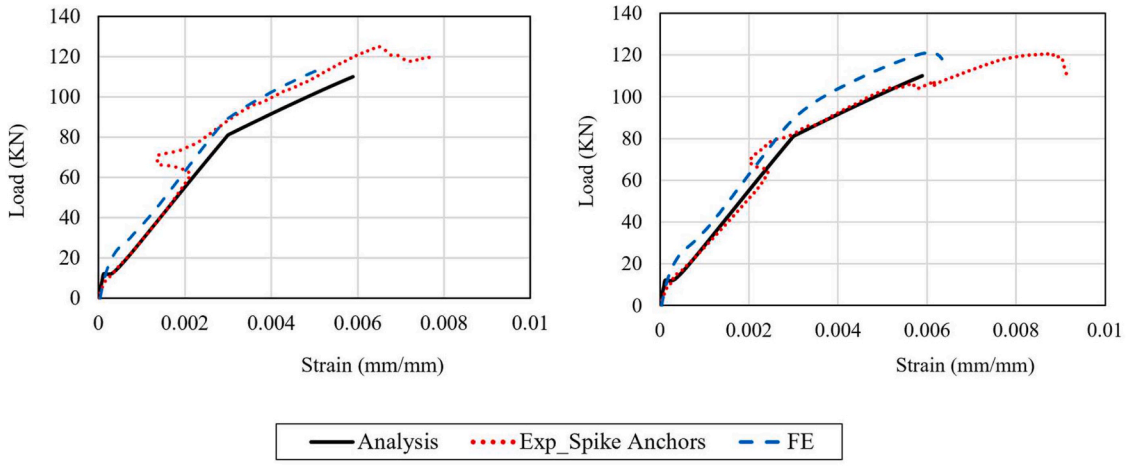

Fig. 19. Comparison between FE and literature [38] of the load-strain in the CFRP sheets for (a) SB16SR beam; and (b) SB19SR.

Table 2
Summary of load capacity and failure modes for different anchor embedment depths.

Embedded depth (mm)	Load (kN)	Failure mode in the CFRP sheet	Failure mode in the CFRP fibre anchors
30	173.92	debonding	pull-out
40	174.03	debonding	pull-out
60	179.81	debonding	pull-out
80	180.49	debonding	pull-out and shear failure
90	182.66	debonding	shear failure
100	182.74	rupture	shear failure

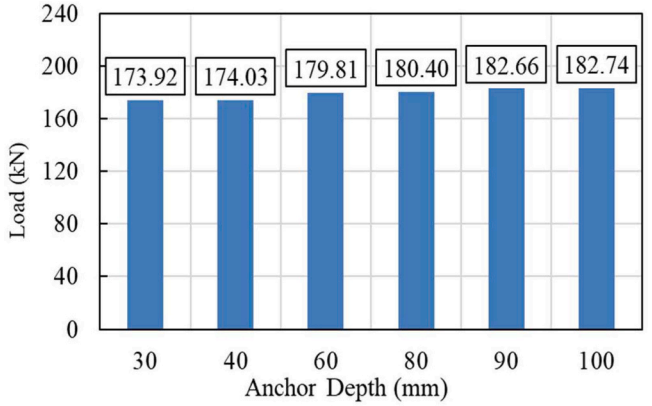

Fig. 20. FE analysis results for different anchor embedment depths.

mechanical interlock. The 100 mm depth achieved the highest load capacity of 182.74 kN and resulted in CFRP rupture, confirming full tensile mobilisation of the strengthening system. The embedment range considered in this study was selected to investigate whether the performance observed at 100 mm, previously reported by Zaki et al. [38], could be approached at reduced depths. While 100 mm had shown favourable behaviour experimentally, the absence of comparative data limited understanding of whether it represented an optimal or conservative choice. The present analysis addressed this through a systematic evaluation of intermediate depths, enabling direct comparison of capacity and failure mechanisms. The results indicate that embedment depths of 90 mm and above are sufficient to eliminate pull-out and achieve effective anchorage. However, only the 100 mm depth ensured full tensile utilisation of the CFRP, highlighting its superior performance. This distinction provides clarity on the minimum embedment required to fully engage the strengthening system under flexural loading.

3.1.2. Impact of anchor spacing on load distribution

The spacing and quantity of CFRP fibre anchors play a significant role in governing stress distribution and failure progression. To assess this influence, FE analyses were carried out using four different anchor spacings: 140 mm, 160 mm, 180 mm, and 220 mm. The total number of anchors decreased accordingly, while the embedment depth was held constant at 100 mm to isolate the effect of spacing alone. The numerical results in Table 3 and Fig. 22 show a consistent decrease in load capacity as anchor spacing increased from 140 mm to 220 mm. This trend reflects the reduced confinement and diminished anchor engagement over the beam length. Although all models shared the same embedment depth and exhibited anchor shear failure, the CFRP sheets exhibited distinct failure modes depending on the spacing configuration.

At 140 mm spacing, CFRP rupture occurred, indicating full utilisation of the laminate's tensile capacity and corresponding to the highest load-bearing performance. Wider spacings of 160 mm, 180 mm, and 220 mm led to premature debonding of the CFRP sheets. These configurations lacked sufficient anchorage density to maintain interfacial stress control, resulting in reduced composite action and delayed strain development in the strengthening system.

The spacings selected in this study reflect practical ranges commonly used in design, yet detailed comparative assessment of their influence on failure mode and tensile engagement of CFRP has remained limited. By quantifying performance across this range, the analysis clarifies the extent to which spacing influences load transfer efficiency and failure progression. The results demonstrate that although all configurations-maintained shear-dominated anchor failure, only the 140 mm spacing was sufficient to activate the full tensile strength of the CFRP, thereby defining an effective spacing threshold for reliable flexural performance. To complement the quantitative results in Table 3, Fig. 23 presents representative FE-predicted failure modes for SB16ST at two anchorage layouts. The configuration with 12 anchors at 140 mm spacing shows clear CFRP sheet rupture, whereas increasing the spacing to 160 mm (11 anchors) leads to the onset of debonding. The accompanying side views emphasise these behaviours by highlighting the rupture zone in the 12-anchor case and the debonding region in the 11-anchor case. Together,

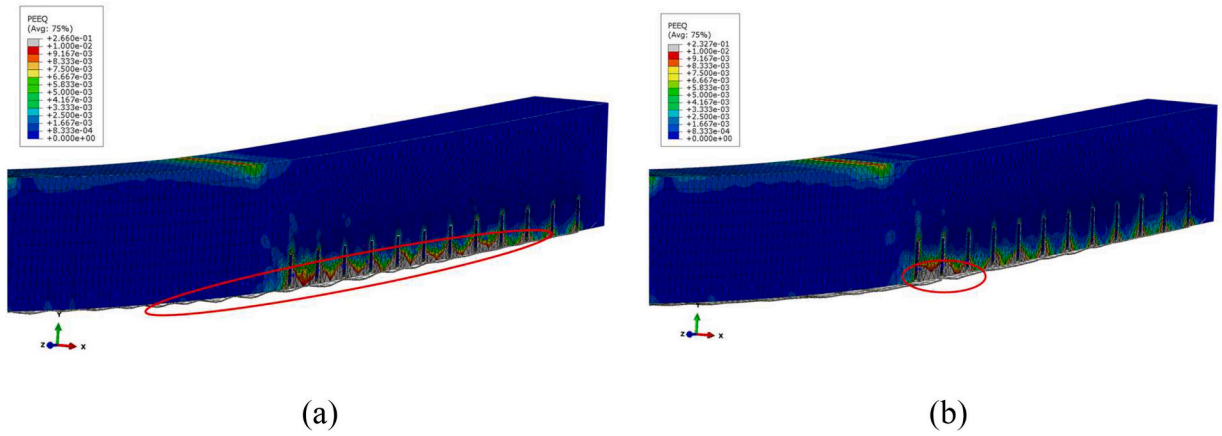

Fig. 21. Comparison of FE-predicted failure modes for SB16ST with (a) 80 mm embedment depth, showing CFRP sheet debonding; and (b) 100 mm embedment depth, showing CFRP sheet rupture.

Table 3
Summary of load capacity and failure modes for different CFRP anchor.

Embedded depth (mm)	Spacing (mm)	Number of anchors	Load (kN)	Failure mode CFRP sheet	Failure mode CFRP fibre anchors
100	140	12	182.74	rupture	shear failure
100	160	11	182.62	debonding	shear failure
100	180	10	178.33	debonding	shear failure
100	220	8	176.45	debonding	shear failure

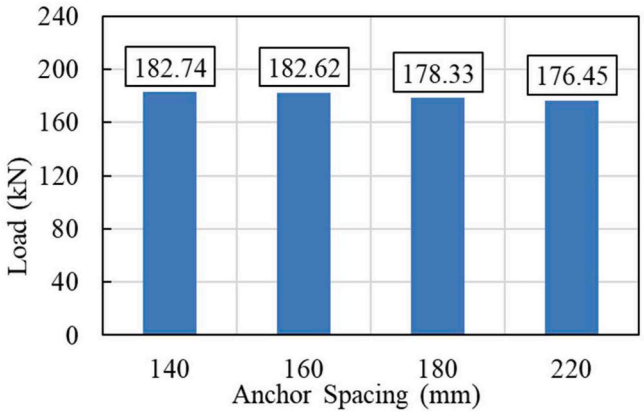

Fig. 22. FE analysis results for different anchor spacings.

these visualisations illustrate the transition from rupture-dominated to debonding-dominated response as anchor spacing increases.

3.1.3. *Influence of end anchor removal on stability*

Strengthened RC beams may fail before the debonding front reaches the outermost CFRP fibre anchors. To examine this behaviour, four anchorage layouts were modelled. The reference configuration included twelve anchors per shear span. The second configuration had eleven anchors by removing one from each end. The third configuration included ten anchors per span by removing two from each end. The fourth configuration considered nine anchors per shear span after removing three anchors from both ends of the beam. All anchors had an embedment depth of 100 mm and were spaced at 140 mm intervals.

As summarised in Table 4 and shown in Fig. 24, removing one anchor from each end caused only a marginal drop in load capacity. The CFRP sheet failed by rupture, and the anchors failed in shear, indicating that the excluded anchors were positioned beyond the effective strain development zone and contributed little to the overall capacity. The reduction in anchors shortened the active anchorage zone and limited interfacial stress transfer, shifting the behaviour toward debonding. The removal of one anchor from either end of the beam therefore produced the desired failure modes, CFRP rupture and anchor shear failure, while additional removal caused premature debonding. In the third configuration, with two anchors removed from each end, the beam exhibited a slightly lower load capacity and failed by partial rupture of the CFRP sheet. This represented an intermediate response between the full rupture observed in configuration 2 and the shear-out failure observed in configuration 4. The intermediate response resulted from limited interfacial stress development due to the reduced anchorage length. The partial rupture observed indicates that tensile stresses in the CFRP were near full mobilisation, but the reduced anchorage prevented complete stress transfer before debonding initiated.

To complement the results in Table 4, Fig. 25 illustrates the FE-predicted failure modes of CFRP sheets for the SB16ST beam in the full-anchor configuration (12 anchors) and the most reduced case (9 anchors). These visualisations highlight the overall transition from CFRP rupture to debonding observed across the end-anchor removal sequence and provide clear examples of the two bounding behaviours identified in the numerical study.

This performance reflects the influence of anchor location on stress development. The outermost anchors in the full-length layout were installed at 152 mm from the beam edge. The fan spread of the anchors extended 140 mm inward, placing the effective reinforcement action up to 292 mm from the edge. The distance from the applied load to the beam edge defines the shear span, which measured 1827 mm. Therefore, the outermost anchor effect commenced at approximately 292 mm, equating to 16 % of the shear span length. This layout is illustrated in Fig. 26. The 16 % ratio defining the ineffective anchorage zone is specific to the full-scale T-shaped beams examined in this study. Although the numerical results clearly indicate that this region was ineffective for the present specimens, its applicability to T-beams with differing spans, flange dimensions, web thicknesses, or reinforcement arrangements has not yet been verified. Variations in these geometric and structural parameters may influence strain development and anchorage effectiveness, and thus further investigation is required before generalising this ratio to other configurations.

The negligible impact of removing the first anchor suggests that up to 292 mm from the edge of the beam did not contribute meaningfully to the ultimate flexural load capacity. This region did not sustain

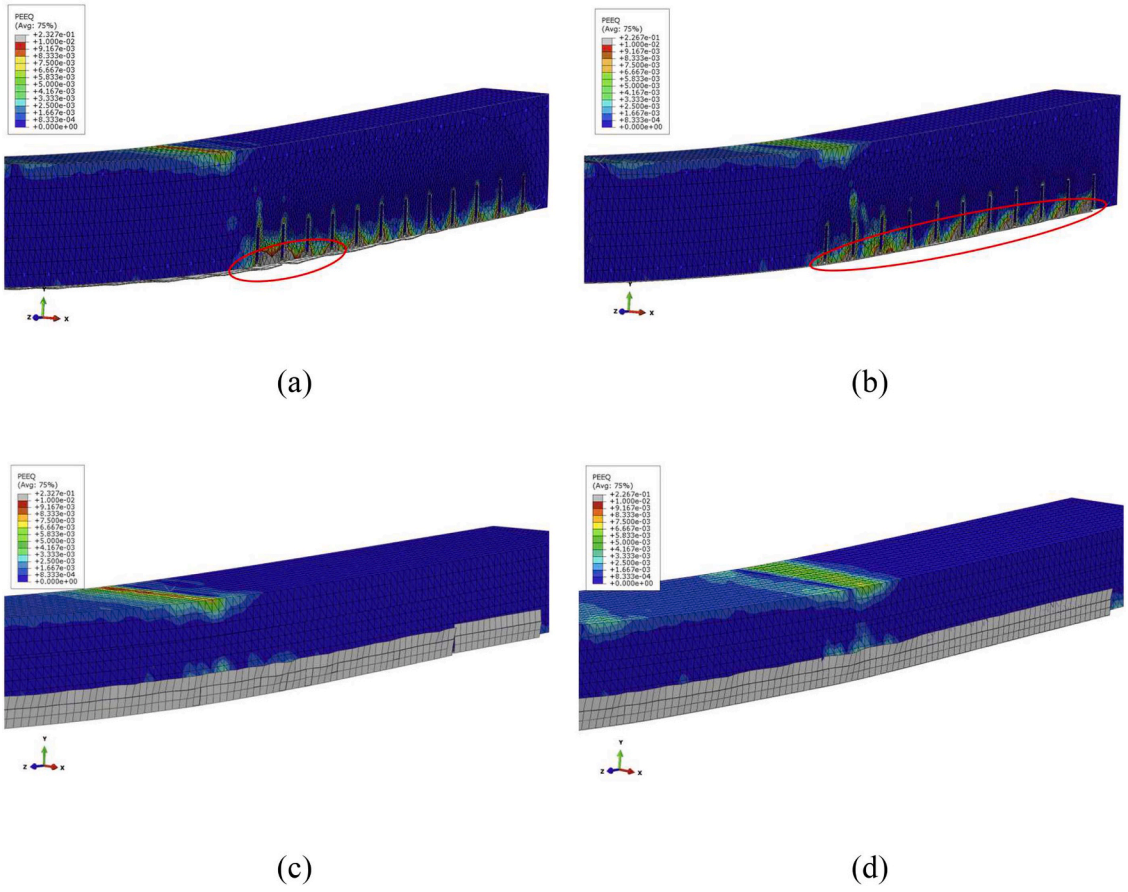

Fig. 23. FE-predicted failure modes for SB16ST under different anchor spacings: (a) 12 anchors at 140 mm spacing, showing CFRP sheet rupture; (b) 11 anchors at 160 mm spacing, showing onset of debonding; (c) side-view of case (a), highlighting the rupture zone; and (d) side-view of case (b), highlighting the debonding region.

Table 4
Summary of load capacity and failure modes for different end anchor offsets.

Embedded depth (mm)	Spacing (mm)	Number of anchors	Anchor offset	Load (kN)	Failure mode CFRP sheet	Failure mode CFRP fibre anchors
100	140	12	0	182.74	rupture	shear failure
100	140	11	1	180.73	rupture	shear failure
100	140	10	2	180.68	partial rupture	shear failure
100	140	9	3	180.48	debonding	shear failure

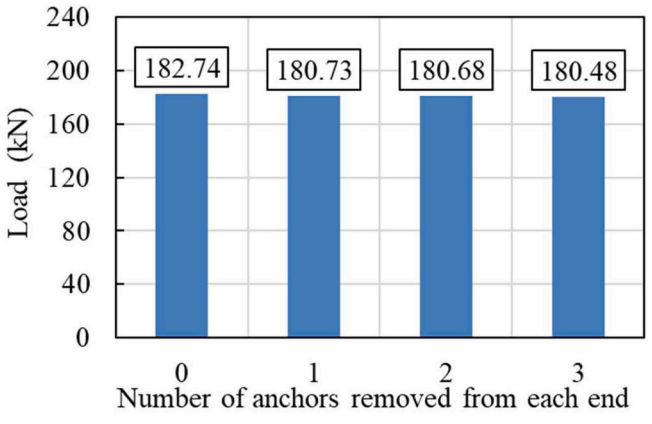

Fig. 24. FE analysis results for different end anchor offsets.

significant strain or develop anchorage tension. Consequently, the first 10 % to 16 % of the shear span acted as a non-effective anchorage zone for flexural beams. The effective anchorage zone was determined from the measured load-response behaviour and the corresponding failure mode observations. As summarised in Table 4, Offsetting or removing end anchors had little effect on the load capacity but caused the CFRP failure mode to transition from rupture to partial or full debonding. The CFRP sheets predominantly failed in rupture, and the fibre anchors failed in shear, indicating that anchors located within approximately the first 10–16 % of the span contribute little to the anchorage efficiency. When two anchors were removed from each end, the CFRP sheet response transitioned from rupture to partial debonding, whereas removing three anchors resulted in full debonding.

This finding is significant. It highlights that anchor placement near the beam end does not enhance capacity unless sufficient strain can develop in the region. Also, this finding is complementary to the previous study by Smith et al. [54] that showed that the fibre anchors in the constant moment region (at the midspan of the beam) have no influence on the flexural capacity. To ensure the efficient use of materials, time,

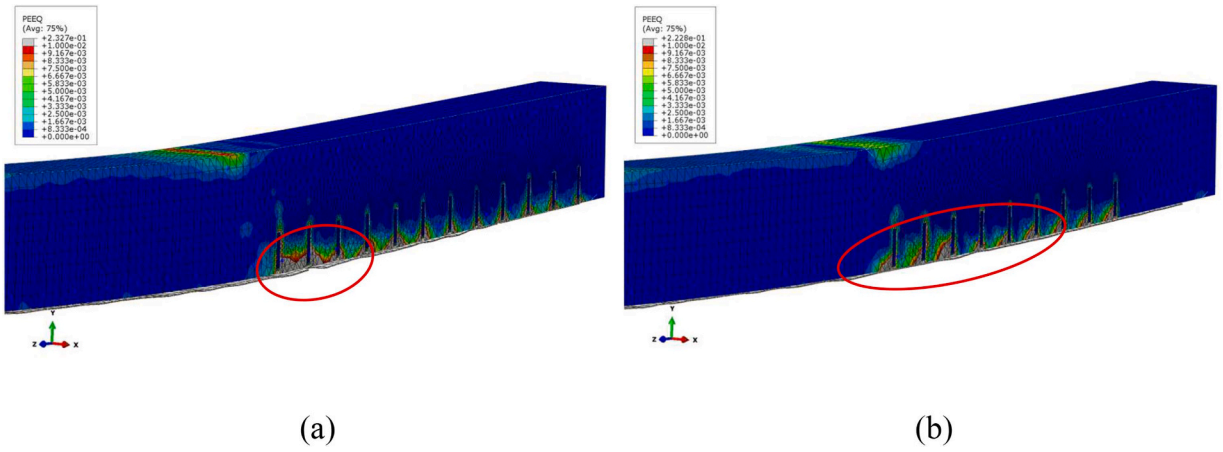

Fig. 25. FE-predicted failure modes of CFRP sheet for SB16ST beams with progressive end-anchor removal: (a) 12 anchors, CFRP rupture; (b) 9 anchors, CFRP debonding.

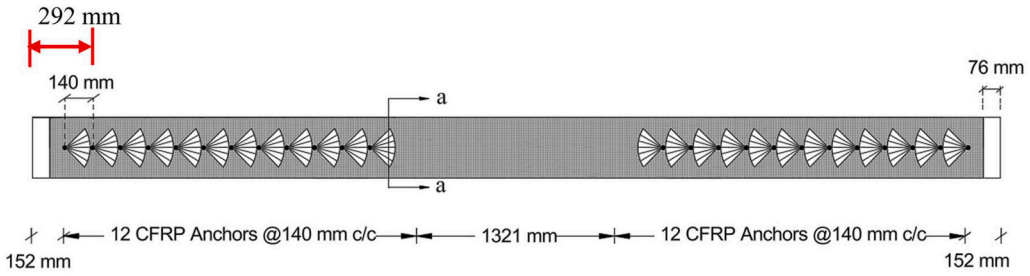

Fig. 26. Schematic layout showing anchor fan extension and effective anchorage zone relative to the shear span.

and overall costs, considerable guidance and support will be provided to researchers and practicing engineers. This will be achieved by installing fibre anchors within 84 % of the shear span, thus optimizing their effectiveness. The results demonstrate a threshold beyond which reducing the anchorage length directly compromises performance. They provide evidence for rationalising anchor distribution by eliminating end-region anchors that do not engage while maintaining strength. This approach improves material efficiency without affecting the structural reliability of the system.

3.2. Rectangular beam parametric analysis

Two rectangular beam configurations were investigated, designated R-305 and R-350, with total web depths of 305 mm and 350 mm, respectively. The R-305 beam matched the web depth of the previously analysed T-beams to enable direct comparison, while R-350 was selected to evaluate the influence of increased web depth. All other parameters, including material properties, reinforcement details, and boundary conditions, were held constant across both rectangular sections and the T-beam models to isolate geometric effects. Each beam was strengthened using twelve CFRP fibre anchors per shear span, with a fixed anchor diameter of 16 mm and spacing of 140 mm, corresponding to the SB16SR anchor configuration. The parametric study focused exclusively on the influence of anchor embedment depth, given the dominant failure mode associated with concrete crushing. Numerical analyses were performed for embedment depths ranging from 30 mm to 130 mm, at 10 mm intervals, yielding a total of eleven cases per section for both R-305 and R-350 beams. Fig. 27 provides a clearer comparison of failure load capacity as a function of anchor embedment depth for sections R-305 and R-350. The results confirm that increasing the embedment depth does not significantly enhance the load-carrying capacity. This trend is consistent across both beam sizes, reinforcing the observation that

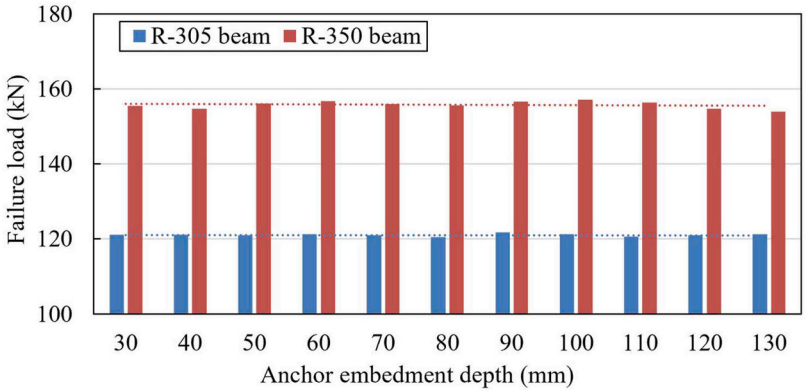

Fig. 27. Load capacity versus anchor embedment depth for rectangular sections.

concrete crushing governs the ultimate failure mode.

The consistent plateau in failure loads across varying anchor depths implies that the CFRP fibre anchors could not be fully mobilised. Their tensile capacity remained underutilised due to the premature crushing of concrete, which acted as the limiting factor. Consequently, deeper anchor installation had little influence on improving the peak capacity.

Nonetheless, the use of fibre anchors in rectangular sections contributes to improved ductility and mitigates premature debonding. Compared to unanchored beams, the anchored specimens show enhanced deformation capacity and a more stable post-peak response, as also observed in earlier studies [55]. This underscores the role of the anchorage system in improving failure control, even when the ultimate capacity is governed by concrete crushing.

3.3. Effect of embedment depth by section type

A comparative analysis was carried out in this section to assess the effect of anchor embedment depth on the performance of T-beams and rectangular beams. In T-beams strengthened with CFRP and subjected to displacement-controlled four-point bending, anchor depth had a clear impact on both load capacity and failure mode. Shallow embedment led to premature debonding of the CFRP sheet and anchor pull-out. As the embedment depth increased, the load capacity improved, and the failure mode shifted to more stable mechanisms such as CFRP rupture and anchor shear-out. These outcomes highlight the critical role of embedment depth in achieving effective tensile mobilisation in T-beam systems.

In contrast, the rectangular beams with web depths of 305 mm and 350 mm showed minimal sensitivity to embedment depth. Across the full range of depths, concrete crushing governed the response and limited the tensile contribution of the anchors. The fibre anchors could not fully engage, and no significant improvement in strength was observed with deeper embedment. This distinction underscores a fundamental difference in how anchor effectiveness is influenced by beam geometry and failure mechanism. For the beams studied herein, an embedment depth (d) of 100 mm, corresponding to 33 % of the total web height (h) of 305 mm, provides a practical design guideline ($d/h = 0.33$). This ratio works well for T-section beams, as they fully utilize the anchor capacity and the failure mode depends on the strengthening and anchorage details. In contrast, rectangular beams are limited by crushing-dominated failure modes. A more generalized ratio for reinforced concrete beams is currently being investigated in ongoing research project by the same authors.

The comparison establishes that while T-beams benefit directly from increased embedment depth, rectangular sections are controlled by compressive failure modes. Fig. 28 illustrates the variation in load capacity with embedment depth across both beam types with 305 mm depth, reinforcing the influence of structural geometry on anchorage performance.

Fig. 28 demonstrates that embedment depth is a critical design parameter for T-beams, contributing to increased load capacity through improved anchor engagement. In contrast, its influence in rectangular beams is negligible, as failure is dominated by concrete crushing, which limits anchor effectiveness.

Although the load plateau in rectangular beams was governed by crushing, anchors still contributed to system behaviour. A minimum embedment of 30 mm was necessary to prevent premature CFRP debonding and ensure full laminate engagement. This anchorage improved stress transfer and slightly enhanced deformation capacity, even though ultimate strength remained unchanged. Numerical strain results validated against experiments confirmed stable CFRP mobilisation up to failure. Additional ductility can be achieved by prestressing the CFRP laminates before bonding [56] and [57]. A tougher adhesive layer can allow gradual slip and delay sudden debonding.

This study focused on the flexural behaviour of CFRP-strengthened beams with fibre anchors under static loading. Durability aspects were not investigated but are critical for long-term performance. Environmental factors such as moisture ingress, freeze–thaw cycles, and temperature variation can alter adhesive behaviour, degrade bond quality, and affect anchor efficiency over time. Repeated or fatigue loading may also change load transfer mechanisms and accelerate debonding. Future work should include controlled studies under these conditions to assess durability and support the development of reliable design guidelines for anchored CFRP systems.

4. Conclusion

This study numerically evaluated the performance of CFRP fibre anchors in reinforced concrete beams using validated finite element models developed in ABAQUS. The main conclusions are as follows:

For T-section beams:

1. The FE models reproduced load-deflection, strain, and failure modes with about 95 % agreement with experiments, confirming their reliability.
2. An embedment depth of 100 mm achieved the highest capacity and caused shear failure of the anchors, preventing pull-out.
3. CFRP rupture occurred at 100 mm embedment, confirming full tensile mobilisation.

An embedment depth equal to a depth-to-height (d/h) ratio of 0.33 proved effective for full anchor mobilisation in the T-section beams studied, providing a practical guideline for design.

1. An optimal 140 mm spacing maintained interfacial control, while wider spacing ($\geq$160 mm) caused premature debonding and reduced strength.

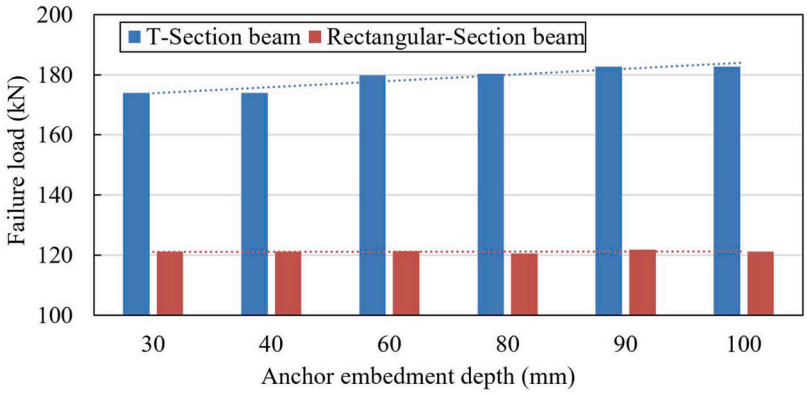

Fig. 28. Load capacity versus embedment depth for both beam types with 305 mm depth.

2. Removing one end anchor from each side had negligible influence (<1 %) on strength, as debonding initiated near the load region.

Effective anchorage began about 292 mm from the beam edge (≈16 % of the shear span); anchors within this zone were non-effective and can be omitted to reduce cost and material use.

For rectangular-section beams:

1. The FE-predicted ultimate load for beam R-305 with 100 mm embedment was 121.1 kN, within 97 % of experimental results.
2. Load-deflection responses for R-305 and R-350 beams were almost identical at all embedment depths, showing minimal sensitivity to this parameter.
3. Increasing beam depth from 305 mm to 350 mm raised capacity but did not alter the failure mode, which remained governed by concrete crushing.
4. Increasing the anchor embedment depth had a negligible effect on improving the load capacity for both R-305 and R-350 beams due to the concrete crushing failure mechanism.

The findings of this study provide clear implications for practical engineering design. The identification of effective embedment depth, optimal anchor spacing, and the extent of ineffective anchorage zones offers quantitative guidance for designing more efficient and economical CFRP strengthening systems. For T-beams, the results demonstrate that full fibre mobilisation can be achieved without excessive anchor use, thereby reducing material demand and improving constructability. In contrast, the limited contribution of anchors in rectangular beams, where failure is governed by concrete crushing, highlights the importance of allocating strengthening resources where they are most structurally effective. These insights collectively support the development of more reliable, cost-efficient, and performance-optimised CFRP strengthening strategies for real-world applications.

Formatting of funding sources

This research was supported by the Institution of Civil Engineers (ICE) through the ICE Research and Development Enabling Fund (Grant No. RDE 2429). Additional support was provided by the University of Hertfordshire and the American University of Dubai.

CRediT authorship contribution statement

Asal Pournaghshband: Writing – review & editing, Writing – original draft, Validation, Software, Resources, Methodology, Funding acquisition, Formal analysis, Conceptualization. **Mohammed A. Zaki:** Writing – review & editing, Writing – original draft, Visualization, Formal analysis.

Declaration of competing interest

During the preparation of this work, the authors used ChatGPT in order to improve the quality of writing, including assistance with proofreading and drafting the manuscript more effectively. After using this tool/service, the authors reviewed and edited the content as needed and take full responsibility for the content of the publication. The authors declare that they have no known competing financial interests or personal relationships that could have appeared to influence the work reported in this paper.

Acknowledgements

The authors gratefully acknowledge the Institution of Civil Engineers (ICE) for funding this research through the ICE Research and Development Enabling Fund (Grant No. RDE 2429). Further appreciation is extended to the University of Hertfordshire, School of Physics, Engineering and Computer Science, for providing access to office space, computational facilities, and ABAQUS research licences. The authors also thank the American University in Dubai for its institutional support during the course of this work.

Data availability

No data was used for the research described in the article.

References

[1] J. Li, J. Gong, L. Wang, Seismic behavior of corrosion-damaged reinforced concrete columns strengthened using combined carbon fiber-reinforced polymer and steel jacket, Constr. Build. Mater. 23 (7) (2009) 2653–2663, https://doi.org/10.1016/j.conbuildmat.2009.01.003. Jul.
[2] Z. Huang, W. Zhang, X. Qian, Z. Su, D.-C. Pham, N. Sridhar, Fatigue behaviour and life prediction of filament wound CFRP pipes based on coupon tests, Mar. Struct. 72 (2020) 102756, https://doi.org/10.1016/j.marstruc.2020.102756. Jul.
[3] Y.G. Kim, Shear Behavior of Reinforced Concrete T-Beams Strengthened with Carbon Fiber Reinforced Polymer (CFRP) Sheets and CFRP Anchors," PhD Dissertation, The University of Texas at Austin, Austin, Texas, 2011.
[4] M.M. Fayyadh, H. Abdul Razak, Impact of design parameters and cycles of damage loads on CFRP repair effectiveness of Shear-Deficient RC structures, Constr. Build. Mater. 347 (2022) 128465, https://doi.org/10.1016/j.conbuildmat.2022.128465. Sep.
[5] Y. Zhu, K. Shen, S. Wan, J.C. Brigham, A. Fascetti, P. Zhou, Torsional repair of damaged single-box multi-cell composite box-girder with corrugated steel webs using CFRP. Part I: experimental investigation, Compos. Struct. 296 (2022) 115920, https://doi.org/10.1016/j.compstruct.2022.115920. Sep.
[6] T. Pan, Y. Zheng, Y. Zhou, Y. Liu, K. Yu, Y. Zhou, Coupled effects of corrosion damage and sustained loading on the flexural behavior of RC beams strengthened with CFRP anchorage system, Compos. Struct. 289 (2022) 115416, https://doi.org/10.1016/j.compstruct.2022.115416. Jun.
[7] J.F. Bonacci, M. Maalej, Behavioral Trends of RC Beams Strengthened with Externally Bonded FRP, J. Compos. Constr. 5 (2) (2001) 102–113, https://doi.org/10.1061/(ASCE)1090-0268(2001)5:2(102). May.
[8] S.L. Orton, J.O. Jirsa, O. Bayrak, Design Considerations of Carbon Fiber Anchors, J. Compos. Constr. 12 (6) (2008) 608–616, https://doi.org/10.1061/(ASCE)1090-0268(2008)12:6(608). Dec.
[9] W. Sun, Behavior of carbon fiber reinforced polymer (CFRP) anchors strengthening reinforced concrete structures," PhD thesis, The University of Texas at Austin, Austin, Texas, 2014.
[10] H. Akbarzadeh Bengar, A.A. Shahmansouri, A new anchorage system for CFRP strips in externally strengthened RC continuous beams, J. Build. Eng. 30 (2020) 101230, https://doi.org/10.1016/j.jobe.2020.101230. Jul.
[11] J. Esmaeili, O.R. Aghdam, K. Andalibi, J. Kasaei, O. Gencel, Experimental and numerical investigations on a novel plate anchorage system to solve FRP debonding problem in the strengthened RC beams, J. Build. Eng. 45 (2022) 103413, https://doi.org/10.1016/j.jobe.2021.103413. Jan.
[12] A. Mostafa, A.G. Razaqpur, CFRP Anchor for Preventing Premature Debonding of Externally Bonded FRP Laminates from Concrete, J. Compos. Constr. 17 (5) (2013) 641–650, https://doi.org/10.1061/(ASCE)CC.1943-5614.0000377. Oct.
[13] R. Kalfat, R. Al-Mahaidi, Improvement of FRP-to-concrete bond performance using bidirectional fiber patch anchors combined with FRP spike anchors, Compos. Struct. 155 (2016) 89–98, https://doi.org/10.1016/j.compstruct.2016.08.010. Nov.
[14] H. Zhang, S.T. Smith, R.J. Gravina, Z. Wang, Modelling of FRP-concrete bonded interfaces containing FRP anchors, Constr. Build. Mater. 139 (2017) 394–402, https://doi.org/10.1016/j.conbuildmat.2017.02.080. May.
[15] R. Kalfat, R. Al-Mahaidi, Mitigation of premature failure of FRP bonded to concrete using mechanical substrate strengthening and FRP spike anchors, Compos. B Eng. 94 (2016) 209–217, https://doi.org/10.1016/j.compositesb.2016.03.062. Jun.
[16] W. Sun, H. Liu, Y. Wang, T. He, Impacts of configurations on the strength of FRP anchors, Compos. Struct. 194 (2018) 126–135, https://doi.org/10.1016/j.compstruct.2018.04.020. Jun.
[17] T. Ozbakkaloglu, M. Saatcioglu, Tensile Behavior of FRP Anchors in Concrete, J. Compos. Constr. 13 (2) (2009) 82–92, https://doi.org/10.1061/(ASCE)1090-0268(2009)13:2(82). Apr.
[18] ACI-440.2R, Guide For the Design and Construction of Externally Bonded FRP Systems for Strengthening Concrete Structures, American Concrete Institute, Farmington Hills, Michigan, USA, 2008.
[19] TR55, Design Guidance for Strengthening Concrete Structures Using Fiber Composite Materials," TR55, 3rd ed, The Concrete Society, Camberley, Surrey, UK, 2012.
[20] CNR-DT-200R1, Guide for the Design and Construction of Externally Bonded FRP Systems for Strengthening Existing Structures. Advisory Committee on Technical Recommendations For Construction, National Research Council, Rome, Italy, 2013.
[21] A.K. Al-Tamimi, R. Hawileh, J. Abdalla, H.A. Rasheed, Effects of Ratio of CFRP Plate Length to Shear Span and End Anchorage on Flexural Behavior of SCC RC Beams, J. Compos. Constr. 15 (6) (2011) 908–919, https://doi.org/10.1061/(ASCE)CC.1943-5614.0000221. Dec.

[22] R. Al-Rousan, M. AL-Tahat, An Anchoring Groove Technique to Enhance the Bond Behavior between Heat-Damaged Concrete and CFRP Composites, Buildings 10 (12) (2020) 232, https://doi.org/10.3390/buildings10120232. Dec.
[23] R.Z. Al-Rousan, M.F. AL-Tahat, Consequence of anchoring holes technique on the bond behavior between CFRP composites and heat-damaged concrete, Structures 27 (2020) 1903–1918, https://doi.org/10.1016/j.istruc.2020.08.023. Oct.
[24] H. Tahsiri, O. Sedehi, A. Khaloo, E.M. Raisi, Experimental study of RC jacketed and CFRP strengthened RC beams, Constr. Build. Mater. 95 (2015) 476–485, https://doi.org/10.1016/j.conbuildmat.2015.07.161. Oct.
[25] A.A. El-Ghandour, Experimental and analytical investigation of CFRP flexural and shear strengthening efficiencies of RC beams, Constr. Build. Mater. 25 (3) (2011) 1419–1429, https://doi.org/10.1016/j.conbuildmat.2010.09.001. Mar.
[26] Y. Zhang, L. Duan, H. Liu, J. Lu, Y. Huo, Experimental and numerical study on multi-impact performance of pre-damaged beams strengthened with CFRP, Eng. Struct. 285 (2023) 116034, https://doi.org/10.1016/j.engstruct.2023.116034. Jun.
[27] Y.O. Özkılıç, C. Aksoylu, Ş. yazman, L. Gemi, M.H. Arslan, Behavior of CFRP-strengthened RC beams with circular web openings in shear zones: numerical study, Structures 41 (2022) 1369–1389, https://doi.org/10.1016/j.istruc.2022.05.061. Jul.
[28] G.M. Chen, Z. Zhang, Y.L. Li, X.Q. Li, C.Y. Zhou, T-section RC beams shear-strengthened with anchored CFRP U-strips, Compos. Struct. 144 (Jun. 2016) 57–79, https://doi.org/10.1016/j.compstruct.2016.02.033.
[29] J.A. Abdalla, H.H. Mhanna, A.B. Ali, R.A. Hawileh, CFRP U-Wraps and Spike Anchors for Enhancing the Flexural Performance of CFRP-Plated RC Beams, Polymers. (Basel) 15 (7) (2023) 1621, https://doi.org/10.3390/polym15071621. Mar.
[30] M. de Freitas Arcine, N. Villanova Menon, P. Augusto Krahl, Numerical and experimental study of the interaction between stirrups and shear strengthening with CFRP in RC beams, Eng. Struct. 278 (2023) 115514, https://doi.org/10.1016/j.engstruct.2022.115514. Mar.
[31] E. del Rey Castillo, R. Kanitkar, S.T. Smith, M.C. Griffith, J.M. Ingham, Design approach for FRP spike anchors in FRP-strengthened RC structures, Compos. Struct. 214 (2019) 23–33, https://doi.org/10.1016/j.compstruct.2019.01.100. Apr.
[32] Z. Huang, et al., Multi-impact performance of prestressed CFRP-strengthened RC beams using H-typed end anchors, Mar. Struct. 85 (2022) 103264, https://doi.org/10.1016/j.marstruc.2022.103264. Sep.
[33] M. Assad, R.A. Hawileh, J.A. Abdalla, Flexural strengthening of reinforced concrete beams with CFRP laminates and spike anchors, Compos. C: Open Access 13 (2024) 100443, https://doi.org/10.1016/j.jcomc.2024.100443. Mar.
[34] Y. Wang, Q. Jia, R. Surahman, X. He, Static and seismic strengthening of RC frame joints by using CFRP sheets with various anchoring methods, J. Build. Eng. 82 (2024) 108309, https://doi.org/10.1016/j.jobe.2023.108309. Apr.
[35] K. Dong, Y. Gao, S. Yang, Z. Yang, J. Jiang, Experimental investigation and analytical prediction on bond behaviour of CFRP-to-concrete interface with FRP anchors, Case Stud. Constr. Mater. 19 (2023) e02510, https://doi.org/10.1016/j.cscm.2023.e02510. Dec.
[36] H.H. Mhanna, R.A. Hawileh, J.A. Abdalla, Shear behavior of RC T-beams externally strengthened with anchored high modulus carbon fiber-reinforced polymer (CFRP) laminates, Compos. Struct. 272 (2021) 114198, https://doi.org/10.1016/j.compstruct.2021.114198. Sep.
[37] W.A. Shekarchi, D.K. Pudleiner, N.K. Alotaibi, W.M. Ghannoum, J.O. Jirsa, Carbon Fiber-Reinforced Polymer Spike Anchor Design Recommendations, ACI. Struct. J. 117 (6) (2020) 171–182, https://doi.org/10.14359/51728065. Nov.
[38] M.A. Zaki, H.A. Rasheed, T. Alkhrdaji, Performance of CFRP-strengthened concrete beams fastened with distributed CFRP dowel and fiber anchors, Compos. B Eng. 176 (2019) 107117, https://doi.org/10.1016/j.compositesb.2019.107117. Nov.
[39] M.A. Zaki, H.A. Rasheed, R.R. Roukerd, M. Raheem, Performance of reinforced concrete T beams strengthened with flexural CFRP sheets and secured using CFRP splay anchors, Eng. Struct. 210 (2020) 110304, https://doi.org/10.1016/j.engstruct.2020.110304. May.
[40] H.A. Rasheed, M.A. Zaki, A.S. Foerster, Efficient bidirectional U-wrap system to anchor CFRP sheets bonded to reinforced concrete T-girders, Structures 38 (2022) 226–236, https://doi.org/10.1016/j.istruc.2022.02.004. Apr.
[41] H.A. Rasheed, M.A. Zaki, M.M. Raheem, Effectiveness of Fiber Anchors in CFRP Flexural Strengthening of RC Girders, J. Compos. Constr. 28 (4) (2024), https://doi.org/10.1061/JCCOF2.CCENG-4367. Aug.
[42] M.A. Zaki, H.A. Rasheed, K. Mitsios, Improvements in lightweight concrete T beams CFRP strengthened and anchored with U-wraps, Struct. Concr. 25 (3) (2024) 2206–2221, https://doi.org/10.1002/suco.202300968. Jun.
[43] Abaqus Software, Dassault Systemes Simulia Corporation, 2023.
[44] B.H.S. Hamah-Ali, M.R.A. Qadir, The effect of different levels of pre-damage loading on the strength and structural behavior of CFRP strengthened R.C. beams: experimental and analytical investigation, PLoS. One 16 (12) (2021) e0261290, https://doi.org/10.1371/journal.pone.0261290. Dec.
[45] A. Sakbana, M. Mashreib, Análisis de elementos finitos de Vigas de Hormigón Armado CFRP, Rev. ing. constr. 35 (2) (2020) 148–169, https://doi.org/10.4067/S0718-50732020000200148. Aug.
[46] X. Yun, L. Gardner, Stress-strain curves for hot-rolled steels, J. Constr. Steel. Res. 133 (2017) 36–46, https://doi.org/10.1016/j.jcsr.2017.01.024. Jun.
[47] A. Hamoda, M. Emara, W. Mansour, Behavior of steel I-beam embedded in normal and steel fiber reinforced concrete incorporating demountable bolted connectors, Compos. B Eng. 174 (2019) 106996, https://doi.org/10.1016/j.compositesb.2019.106996. Oct.
[48] D.J. Carreira, K.H. Chu, Stress-Strain Relationship for Plain Concrete in Compression, ACI J.l Proc. 82 (6) (1985), https://doi.org/10.14359/10390.
[49] D.J. Carreira, K.H. Chu, Stress-Strain Relationship for Reinforced Concrete in Tension, ACI J. Proc. 83 (1) (1986), https://doi.org/10.14359/1756.
[50] W. Mansour, W. Li, P. Wang, M. Badawi, Experimental and numerical evaluations of the shear performance of recycled aggregate RC beams strengthened using CFRP sheets, Eng. Struct. 301 (2024) 117368, https://doi.org/10.1016/j.engstruct.2023.117368. Feb.
[51] P. Mahrenholtz, J.-Y. Cho, J.-M. Park, R. Eligehausen, Characterization of Shear Strength of FRP Anchors, MATEC Web Conf. 199 (2018) 09008, https://doi.org/10.1051/matecconf/201819909008. Oct.
[52] Y.T. Obaidat, S. Heyden, O. Dahlblom, Evaluation of Parameters of Bond Action between FRP and Concrete, J. Compos. Constr. 17 (5) (2013) 626–635, https://doi.org/10.1061/(ASCE)CC.1943-5614.0000378. Oct.
[53] Y.M. Saeed, W.A. Aules, F.N. Rad, A.M. Raad, Tensile behavior of FRP anchors made from CFRP ropes epoxy-bonded to uncracked concrete for flexural strengthening of RC columns, Case Stud. Constr. Mater. 13 (2020) e00435, https://doi.org/10.1016/j.cscm.2020.e00435. Dec.
[54] S.T. Smith, S. Hu, S.J. Kim, R. Seracino, FRP-strengthened RC slabs anchored with FRP anchors, Eng. Struct. 33 (4) (2011) 1075–1087, https://doi.org/10.1016/j.engstruct.2010.11.018. Apr.
[55] M.A. Zaki, H.A. Rasheed, Impact of efficiency and practicality of CFRP anchor installation techniques on the performance of RC beams strengthened with CFRP sheets, Can. J. Civ. Eng. 46 (9) (2019) 796–809, https://doi.org/10.1139/cjce-2018-0560. Sep.
[56] Y.J. Kim, C. Shi, M.F. Green, Ductility and cracking behavior of prestressed concrete beams strengthened with prestressed CFRP sheets, J. Compos. Constr. 12 (3) (2008) 274–283, https://doi.org/10.1061/(ASCE)1090-0268(2008)12:3(274). Jun.
[57] A. Abdel Havez, A. Al-Mayah, Flexural strengthening of concrete structures using externally bonded and unbonded prestressed CFRP laminates: a literature review, J. Compos. Constr. 27 (4) (2023) 04023012, https://doi.org/10.1061/JCCOF2.CCENG-4053. May.